



**HAL**  
open science

## The 3MI Level-1C geoprojected product - definition and processing description

Ruediger Lang, Gabriele Poli, Bertrand Fougnie, Antoine Lacan, Thierry Marbach, Jérôme Riedi, Peter Schlüssel, André B. Couto, Rosemary Munro

### ► To cite this version:

Ruediger Lang, Gabriele Poli, Bertrand Fougnie, Antoine Lacan, Thierry Marbach, et al.. The 3MI Level-1C geoprojected product - definition and processing description. *Journal of Quantitative Spectroscopy and Radiative Transfer*, 2019, 225, pp.91-109. 10.1016/j.jqsrt.2018.12.022 . insu-03686279

**HAL Id: insu-03686279**

**<https://insu.hal.science/insu-03686279>**

Submitted on 3 Jun 2022

**HAL** is a multi-disciplinary open access archive for the deposit and dissemination of scientific research documents, whether they are published or not. The documents may come from teaching and research institutions in France or abroad, or from public or private research centers.

L'archive ouverte pluridisciplinaire **HAL**, est destinée au dépôt et à la diffusion de documents scientifiques de niveau recherche, publiés ou non, émanant des établissements d'enseignement et de recherche français ou étrangers, des laboratoires publics ou privés.



Distributed under a Creative Commons Attribution 4.0 International License



Contents lists available at ScienceDirect

## Journal of Quantitative Spectroscopy &amp; Radiative Transfer

journal homepage: [www.elsevier.com/locate/jqsrt](http://www.elsevier.com/locate/jqsrt)

# The 3MI Level-1C geoprojected product – definition and processing description



Ruediger Lang<sup>a,\*</sup>, Gabriele Poli<sup>a</sup>, Bertrand Fougnie<sup>a</sup>, Antoine Lacan<sup>a</sup>, Thierry Marbach<sup>a</sup>, Jérôme Riedi<sup>b</sup>, Peter Schlüssel<sup>a</sup>, André B. Couto<sup>a</sup>, Rosemary Munro<sup>a</sup>

<sup>a</sup>EUMETSAT, Darmstadt, Germany

<sup>b</sup>Laboratoire d'Optique Atmosphérique, Université de Lille / CNRS, France

## ARTICLE INFO

### Article history:

Received 22 August 2018

Revised 19 December 2018

Accepted 19 December 2018

Available online 20 December 2018

## ABSTRACT

The Multi-viewing, Multi-channel and Multi-polarisation Imager (3MI) on board the Metop-SG satellites will observe polarised multi-spectral radiances of a single target within a very short time period from the visible to the shortwave infrared region with daily global coverage. In order to provide the users of 3MI data with an easy to use and well characterised radiance product EUMETSAT will make a geoprojected and regridded 3MI level-1C product available to users within 70 min of sensing. The paper describes the methodologies of geoprojection and regridding used for the processing of such a product. In addition, the colocation of ancillary information, in particular from the METimage 20-channel imager providing subpixel information of the radiance field and of clouds is described in detail. The latter information is provided as collocated geometric average values in the product and is also used to provide a realistic scene-dependent error introduced by the radiance regridding. Initial estimates, using a synthetic test dataset of top-of-atmosphere radiances of 3MI and METimage at native instrument resolution, provide an upper limit for the additional radiance error contribution depending on the scene homogeneity. Collocated METimage cloud-top height information is also used for parallax correction of the coregistered radiance data either to the cloud height or to the surface elevation, depending on the origin of the dominant radiance signal within the line-of-sight.

© 2018 The Authors. Published by Elsevier Ltd.

This is an open access article under the CC BY license. (<http://creativecommons.org/licenses/by/4.0/>)

## 1. Introduction

Characterising the interaction of dry and wet atmospheric particles (aerosols and clouds) and their microphysical properties requires the measurement of multi-spectral, polarised radiances over a wide range of scattering angles, in order to maximize the number of independent pieces of information which can be simultaneously retrieved on particle properties [18,15]. Multi-angle observations also support the sampling or screening of angular scattering features such as rainbow and glint and allow the assessment of effects of geometrical structures (such as cloud extent and shadowing effects). In addition multi-angle polarised measurements allow the characterisation of surfaces through the derivation of their polarized bidirectional reflectance distribution function [13].

Ideally, for an accurate retrieval of aerosol and cloud properties, simultaneous polarised and total radiance measurements of a single target under a wide range of observation angles would

be required. Although instrument concepts for simultaneous polarised light measurements exist [19] they have not yet been flown on a satellite platform, and to date no satellite instrument concept for simultaneous multi-angle observation of a single target exists. The SPEXone instrument, using a spectral modulation technology with simultaneous polarised light measurements, is now selected for the NASA PACE mission, to be launched in the timeframe of 2022–2023 [20], together with a second snapshot polarimeter, the HARP-2 instrument, and the Multi-Angle Imager for Aerosols (MAIA), to be launched in the timeframe of 2021, will also provide near-instantaneous polarization measurements at a rate of 28 Hz [4]. For an overview of polarimetric remote sensing missions we refer to [5]. The Multi-viewing, Multi-channel, Multi-polarisation Imager, 3MI, to be flown as part of the EUMETSATs Polar System second generation (EPS-SG) on board the Metop-SG satellites, with a targeted launch in 2022, will observe polarised multi-spectral radiances of a single target within a very short time period from the visible to the shortwave infrared region, and will provide daily global coverage.

\* Corresponding author.

E-mail address: [ruediger.lang@eumetsat.int](mailto:ruediger.lang@eumetsat.int) (R. Lang).

The EPS satellites and their space-borne sensors were defined to support operational meteorology, climate monitoring, and other environmental services from low earth orbiting systems, complementary to geostationary systems such as the Meteosat family of satellites. In this context, EPS has provided continuous observations of the atmosphere at the global Earth scale since 2006. The opportunity to take advantage of polarimetric measurements in this framework was brought forward when defining the EPS-SG satellites and sensors [17]. As a consequence, 3MI, an improved follow-on of the POLDER sensors, was proposed to fly with other sensors designed to provide more continuity with the first generation of EPS sensors (e.g. IASI-NG, METImage, and others) [12]. In this context 3MI will provide new improved polarimetric data in a completely operational and long-term framework, with the EPS-SG system providing a series of 3 identical platforms and sensors, each of which have a lifetime of 7.5 years.

The multi-viewing, multi-channel and multi-polarisation concept of 3MI is characterised by its wide instantaneous field of view (IFOV) across-track (ACT) and along-track (ALT) of  $2200 \times 2200 \text{ km}^2$  thanks to its focal plane 2D-CCD detector measuring visible to near-infrared (VNIR) radiation, and an IFOV covering  $2200 \times 1100 \text{ km}^2$  through its 2D-CMOS shortwave infrared (SWIR) detector [14]. The spatial sampling distance at Nadir is 4 km (which becomes approximately 5.5 and 9 km at the border and at the corner of the VNIR footprint respectively). The instrument is equipped with a single filter wheel with separate optical paths for the two optical heads. The VNIR detector is used to acquire 9 spectral bands in the region of 410 to 910 nm, out of which 6 bands are also measuring the associated state of linear polarisation. The SWIR detector is covering 3 bands between 1350 and 2210 nm, all of which provide also polarisation information.

As the satellite moves along its orbit with a ground-speed of about 7 km/s, a full acquisition sequence is performed, for one given band, every 22 s comprising four cycles of the filter wheel (two of which are without acquisitions – see Table 1). Consequently, the two IFOVs of the instruments will move by approximately 154 km ALT on the Earth surface, from one acquisition to the next for a given spectral band. In this way it is possible to observe any point on the Earth's surface within the instrument ACT under at least 14 different viewing geometries, with about  $9^\circ$  separating each of the VNIR acquisitions. For SWIR channels, additional intermediate acquisitions are made every 11 s comprising two turns of the filter wheel (two turns without acquisitions) in order to mitigate the more limited ALT swath for the SWIR optical head, leading also to 14 different viewing geometries but with about  $4.5^\circ$  separating each of them and a narrower angular sampling range. For more details on the instrument design we refer to [12].

Because of the rotating filter wheel, 3MI measurements of the two optical heads are fully sequential in time. The measurement of radiation for each polarised channel is performed through linear polarisers oriented at  $-60^\circ$ ,  $0^\circ$  and  $60^\circ$  from the reference direction with a temporal separation of 0.25 s while all spectral bands are acquired within 5.5 s corresponding to the duration of one filter wheel turn (Table 1). Eventually, multiple observations of a single target on ground under various observation angles are acquired over a period of about five minutes.

These sequentially acquired measurements require an accurate coregistration of the multi-spectral multi-angle polarised radiance information for a single target on ground. This process has to be carried out as accurately as possible in order to minimise the introduction of radiometric errors due to regriding. Moreover these errors need to be characterised as accurately as possible, so that they may be introduced in the end-to-end error budget provided with each 3MI level-1C product, i.e. calibrated and geometrically rectified Stokes vector components. The accurate coregistration and

regridding of measured radiances to a single target on ground and the provision of an accurate radiometric error is the main task of the 3MI level-1C processing of which concept is described in this paper.

In addition, the 3MI level-1C product exploits the synergy of 3MI with other instruments on board the EPS-SG platform to provide useful ancillary data used in retrievals of aerosol and cloud properties. In particular the 3MI processing makes use of concurrent METImage measurements. METImage is a 20 channels cross-track scanning imaging spectroradiometer measuring reflected solar and emitted terrestrial radiation in the visible to infrared spectral domain between 0.443 and  $13.345 \mu\text{m}$  providing simultaneous and near-simultaneous subpixel information at a spatial sampling of 500 m at Nadir [16] and therefore allows for the characterisation of the 3MI subpixel homogeneity of the observed radiance field, and for an accurate and flexible treatment of clouds observed under largely similar observation conditions.

The paper will first describe the individual tasks of the 3MI level-1C processing in general terms starting with a description of the relevant aspects of the instrument observation concept and the content of the level-1B product used as a starting point of level-1C processing. We then proceed with a description of the core regriding task of the level-1C processor and will introduce the concept of “overlaps” designed specifically for the needs of a near-real time operational processing system. Then we describe how the large amount of angular information which needs to be provided to the users is efficiently reduced in the product without significant loss of accuracy or flexibility. The accurate collocation of ancillary data, in particular from METImage, is described followed by the level-1C processing strategy to correct the coregistered radiances for the parallax effect, both under cloud free and cloudy conditions. Finally we describe a semi-empirical approach to characterise the error introduced on the radiometry by regriding and interpolation of radiance data taking both scene and sensor characteristics into account. In the last section of this paper we summarize a few examples of main 3MI level-1C product parameters derived from one orbit in February 2008 from the synthetic test data and add some concluding remarks.

## 2. The 3MI Level-1B product and a 3MI synthetic top-of-atmosphere test dataset

The 3MI level-1B data product is input to the 3MI level-1B to 1C processing (Table 2). 3MI level-1B data provide top-of-atmosphere Stokes vector components of total and linearly polarised radiances in the native instrument acquisition geometry. The 3MI level-1B product is described in detail in [12].

The results presented here rely on a synthetic test dataset of top-of-atmosphere (TOA) radiances of 3MI geoprojected using its native acquisition geometry and in this way mimicking the 3MI level-1B product. The observation geometry used for the test-data corresponds to three orbits of Metop-A with realistic cloud fields provided by the Advanced Very High Resolution Radiometer (AVHRR) on Metop-A. In addition the TOA radiances as observed by METImage have also been simulated at their native instrument resolution and for the same orbits. The test data simulation software is based on a precise description of orbits and instrument models capturing the main assumptions of both the 3MI and METImage designs. In particular for 3MI, the channel layout on both filter wheels and the measurement timeline have been implemented to realistically represent the acquisition sequence. Then for each individual FOV acquisition, the line of sight for each pixel of the VNIR and SWIR detector arrays have been computed and used to determine intersects with the Earth ellipsoid from which geolocation, sun and viewing geometries were computed. Based on this information, a highly realistic description of the Earth sur-

**Table 1**

3MI filter wheel acquisition sequence of four full filter wheel turns of 5.25 sec each. There are two full turns during which no measurements are taken ("free wheeling"). The integration time per filter for the VNIR and SWIR optical heads – and where applicable for the polarisation P1, P2, P3 (–60°, 0° and 60°) – is about 40 ms. Note that the 910 channel of the SWIR optical head is used for co-registration purposes only and is not available in the level-1 products.

Time instant nr.	Sequence timeline [sec]	VNIR Acquisitions (channel, polarizer)	SWIR Acquisitions (channel, polarizer)
0	0.0	Shutter	shutter
1	0.25	490 P1	
2	0.5	490 P2	
3	0.75	490 P3	
4	1.0	555 P1	1370 P1
5	1.25	555 P2	1370 P2
6	1.5	555 P3	1370 P3
7	1.75	410 P1	
8	2.0	410 P2	
9	2.25	410 P3	
10	2.5	670 P1	2130 P1
11	2.75	670 P2	2130 P2
12	3.0	670 P3	2130 P3
13	3.25	443 P1	
14	3.5	443 P2	
15	3.75	443 P3	
16	4.0	865 P1	1650 P1
17	4.25	865 P2	1650 P2
18	4.5	865 P3	1650 P3
19	4.75	763	
20	5.0	910	(910)
21	5.25	765	
	5.25–11.5	...free wheeling / no acquisition ...	
22	12.5		1370 P1
23	12.75		1370 P2
24	13.0		1370 P3
25	14.0		2130 P1
26	14.25		2130 P2
27	14.75		2130 P3
28	15.5		1650 P1
29	15.75		1650 P2
30	16.0		1650 P3
31	16.5		(910)
	16.75–22.0	...free wheeling / no acquisition ...	

**Table 2**

3MI operational product levels and their content.

3MI product level	Description
0	Raw instrument data
1B	Calibrated and geo-located radiance data for individual 3MI images
1C	Co-located and co-registered radiance data for all 3MI observation angles at a given fixed geo-location grid-point.
2	Geophysical parameters (cloud, aerosol, ...)

face/atmosphere properties was produced for each ground target including surface anisotropic reflectance models (land and ocean), vertical profiles of both aerosol and cloud distributions and their optical properties, and description of atmosphere meteorological thermodynamic states among others. Aerosol information in particular was obtained from the aerosol MACC reanalysis whereas cloud properties are described using a combination of AVHRR derived cloud products and ECMWF reanalysis for the description of water content vertical distribution. Information on cloud fields and surface properties are provided at a high resolution corresponding to the instrument native resolution whereas aerosol and meteorological parameters fields have coarser resolution corresponding to model outputs. Those information were set as input to a radiative transfer simulation software (ARTDECO<sup>1</sup>) in order to compute TOA radiances observable from the instrument. The end-to-end simulation results in a highly realistic test dataset at L1B that can be used to test the L1C processor described in this paper. A description of the test dataset is provided in [8].

Fig. 1 shows synthetic TOA radiance information as would be provided by the 3MI level-1B product geoprojected to the native

acquisition geometry of the 3MI instrument and for a channel of the VNIR optical head at 443 nm and of the SWIR optical head at 2130 nm. The results are provided both in the L1B and in the L1C product as unitless reflectance factor values  $R_f$  per spectral channel with

$$R_f = \pi \frac{L}{F_0} d^2,$$

where  $L$  are reflected Earthshine radiances and  $F_0$  is the channel integrated solar irradiance constant at TOA at the time of the acquisition, corrected for sun-earth distance  $d$  variations in astronomical units. Since the 3MI instrument measures radiance values through linear polarisers arranged at 0°, –60° and 60°, the corresponding Stokes vector components  $I$ ,  $Q$  and  $U$  are derived by applying the Muller matrix coefficients for all detector pixels of the instrument as described in [12]. The 3MI product therefore provides reflectance factor values for these Stokes vector components  $I$ ,  $Q$ ,  $U$  and their corresponding radiometric errors separately and they have to be divided by the cosine of the solar zenith angle to obtain values of reflectance. From these radiances the frequently used degree of linear polarisation (DoLP) can easily be calculated

<sup>1</sup> <http://www.icare.univ-lille1.fr/projects/artdeco>

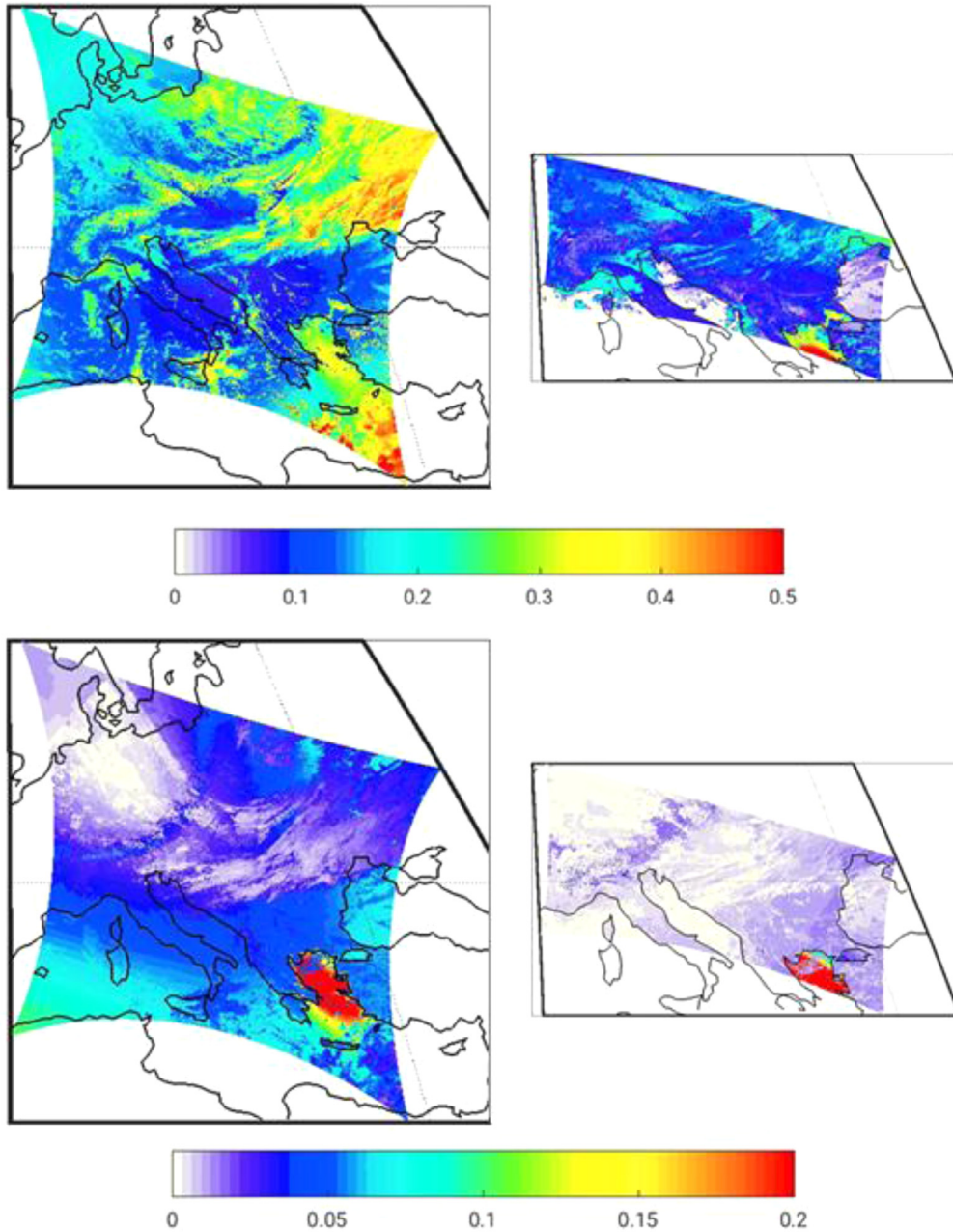


**Fig. 1.** TOA radiance information from the synthetic 3MI test dataset provided in reflectance factor values as in the 3MI level-1B product. The top row shows total reflectances for the 443 nm band (left column) VNIR and for the 2130 nm band (right column) of the SWIR optical head of the instrument for one IFOV of each channel acquired simultaneously during the same filter wheel turn. The lower row shows the same but for the corresponding polarised reflectances  $P$ .

as

$$\text{DoLP} = \frac{\sqrt{Q^2 + U^2}}{I}.$$

Fig. 1 shows total reflectance factor values derived from  $I$  and the corresponding polarised reflectance factors of  $P$  for both channels, where  $P$  is defined as the square root sum of the reflectance factor values for  $Q$  and  $U$ .

### 3. The Level-1C concept

Users of 3MI level-1 radiance data for the retrieval of geophysical properties will often need to relate multiple 3MI measurements to a given geolocation for all spectral channels, including the three

Stokes vector components and for the full range of available observation geometries. Since this coregistration of the temporal sequence of 3MI radiances is not straightforward, there is a clear user need to make such data available in a well-defined way, on an easy to handle fixed geo-projection grid and including a complete characterisation of the associated regridding errors. At the same time, the multi-dimensionality of such data calls for a user-friendly geolocated product including ancillary data such as terrain height or ancillary information from other sensors on EPS-SG, e.g. from METimage.

The 3MI level-1C product processing therefore comprises:

- The geoprojection of 3MI IFOV data (L1B) onto a fixed geo-reference grid (Section 4);

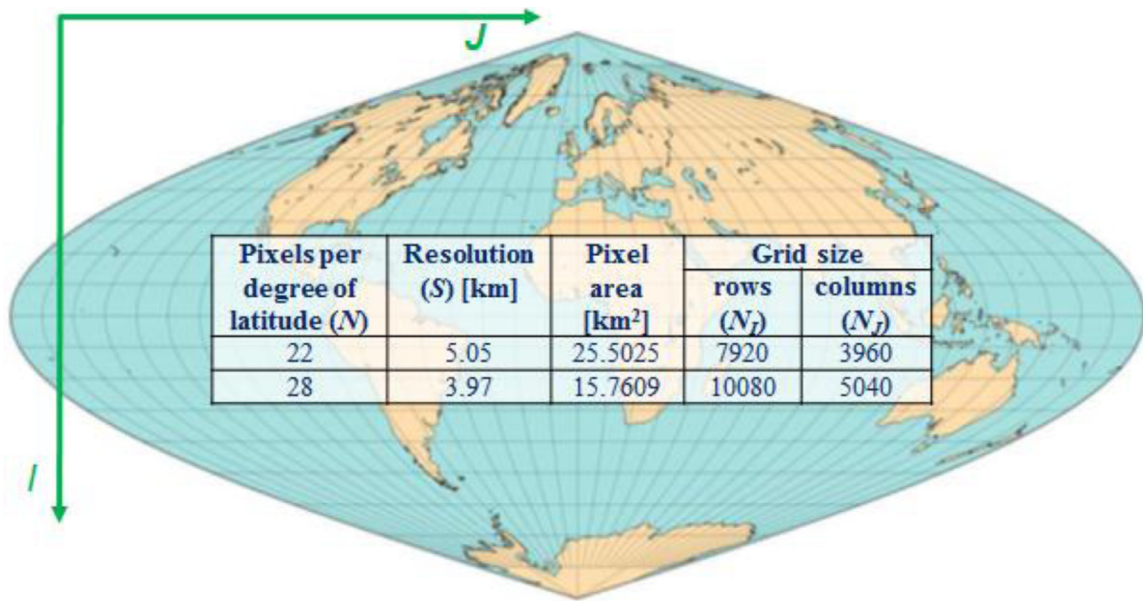


**Fig. 2.** A fixed sinusoidal grid (Sanson-Flamsteed projection) is the chosen reference for the coregistration. By default, the grid configuration of 28 points per degree of latitude is chosen, so that the point size is close to the nominal Nadir ground resolution of the instrument (4 km). But any other configuration can potentially be applied for the level-1C processing without changes to the processing itself.

- The coregistration and regriding of observation data to the fixed grid in a limited target “overlap” region to facilitate fast near real time data dissemination (Section 5);
- The efficient provision of accurate information on the observation geometry for all individual measurements (Section 6);
- The colocation of ancillary data and its use for parallax correction and additional scene information also included in the former (Section 7 and 8);
- The estimation of the radiometric errors associated with geoprojection and regriding depending on observation conditions (Section 9).

#### 4. Geoprojection of data

The level 1C processing uses geo-referenced fully calibrated radiances at the instrument native resolution (level-1B data) and projects them to a common grid. Note that the multi-polarisation measurements taken by the instrument at three different polarisation angles ( $-60^\circ$ ,  $0^\circ$  and  $60^\circ$ ) are already coregistered at level 1B, providing the full Stokes vector in  $I$ ,  $Q$ , and  $U$  at every observation angle and for 9 out of 12 spectral channels [12].

The geoprojection is done with respect to a fixed grid sinusoidal Sanson-Flamsteed projection (Fig. 2), which already has been used before as target reference grid for POLDER and PARASOL level-1C products [3]. The sinusoidal Sanson-Flamsteed projection has been chosen mainly because of its equal area properties and the flexibility of its pixel size configuration (set by default as close as possible to the nominal Nadir ground resolution of the instrument, i.e. at approx. 4 km sampling distance).

In order to achieve an accurate geoprojection to the fixed grid, the 3MI L1B to 1C processor uses a strategy of “inverse” location from the pixel centre of a defined overlap area back to the instrument detector surface (see Fig. 3). The “inverse” location procedure aims at calculating the coordinates (generally fractional) of the focal plane pixel “C” associated with a target pixel “O”.

This procedure therefore includes the transformation of line of sight (LOS) vectors into pointing angles in the satellite nominal reference frame and finally in the instrument reference frame, thus requiring an accurate knowledge of the satellite orbital and atti-

tude parameters, of any instrument mounting offset, and of the focal plane model (i.e. an invertible relation between each focal plane pixel’s coordinates and the respective pointing angles, which takes into account all the effects of the instrument optics).

The tools used to perform the inverse location (as well as other geometrical calculations such as orbital and attitude propagation) are the EO-CFI libraries, provided by ESA and maintained for several earth observing missions (including EPS-SG) [6,7]. The operational and precise information on the satellite orbital parameters are provided by EUMETSAT. The pointing accuracy of the instrument will be characterised on-ground and also regularly checked in-flight, which requires the monitoring of any potential mounting and pointing offset of the instrument.

A specific test has been carried out to assess the intrinsic accuracy of the inverse location function provided by the EO-CFI library. Taking as a reference a simplified instrument focal plane model, for several focal plane pixels the corresponding line of sight (as elevation and azimuth of pointing) and geolocation of the target on the ground have been calculated (i.e. direct location). Then, from the ground target, the line of sight to the satellite is calculated through the inverse location function and compared with the initial line of sight. The comparison shows that the “inverted” line of sight is basically identical to the “direct” one (with an absolute difference of the order of  $10^{-9}^\circ$ ), thus confirming that the error introduced by the inverse location function is negligible. At the same time, the on-ground characterised pointing accuracy of the instrument optics can be verified only to approximately a tenth of the instrument resolving power, using reference measurements, such as those from METImage with significantly higher spatial sampling (approximately 500 m compared to 4 km of 3MI at Nadir). This means that the theoretical accuracy of the inverse location method is about four orders of magnitude higher than the pointing knowledge of the instrument and can therefore be neglected with respect to the latter.

While the intrinsic accuracy of the inverse location method is very high, it is therefore limited by the knowledge of the instrument pointing accuracy. And in contrast to image matching techniques, the inverse location method however does not benefit from any compensation of errors or any auto-correction of instrument

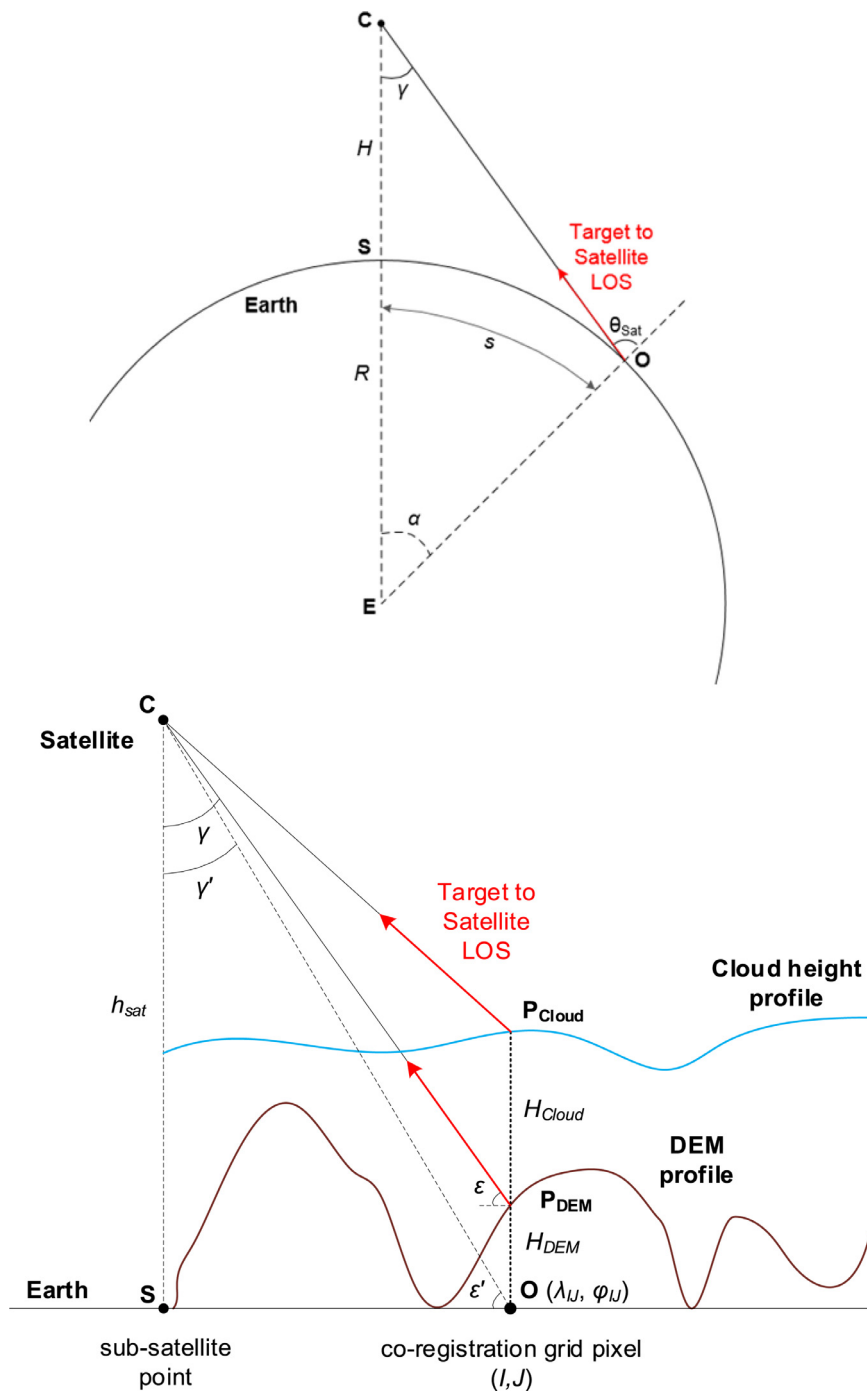


**Fig. 3.** Top panel: Inverse location strategy. A particular line of sight (LOS) angle  $\gamma$  is defined from an arbitrary target “O” on the Earth surface back to the focal plane instrument, thus deriving the fractional coordinates of the focal plane pixel which would have sensed the target O. Lower panel: For the parallax correction of the LOS angle  $\gamma$  to  $\gamma'$  the geodetic height of target O is taken into account using ancillary information (geoid, digital elevation model terrain altitude or cloud top or scattering layer height).

aging (or similar) effects linked to the knowledge of instrument pointing accuracy. The high intrinsic accuracy of the method also comes with the downside of initially higher computational costs per individual signal registration, since the registration has to be carried out for each target pixel individually, and not, like most image matching techniques, for all or for a large number of pixels at once.

The use of the inverse location technique on the other hand allows the so-called parallax correction to be performed at no addi-

tional cost, making the end-to-end processing of coregistered and parallax corrected signals both accurate and efficient. This is shown in the lower panel of Fig. 3. In order to take into account the height above the surface of a grid point O (e.g. the actual elevation or the cloud-top height, which are standard input from the DEM and the METimage cloud parameters), it is sufficient to define the LOS from the actual geodetic height of the target ( $R + P_x$ ), instead of the ellipsoid surface ( $R$ ). For more details on parallax correction Section 8.

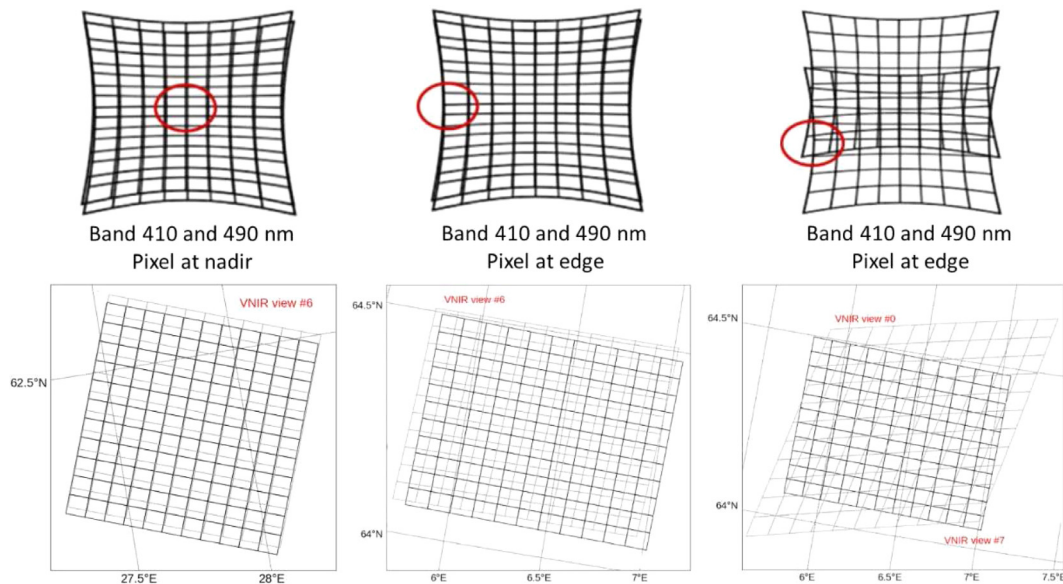


**Fig. 4.** Examples of overlapping ground footprints of super pixels of roughly 11 by 11 detector pixels (lower row) of subsequent instrument acquisitions. The top row shows the position of the super-pixels on the IFOV. The left and middle columns show examples of overlaps for different spectral bands at the same viewing angle and at different positions in the IFOV. The right column shows the footprint for the same band acquired for different views. Overlapping footprints of super-pixel for two different acquisitions are shown in black and light grey in the lower row.

## 5. Coregistration, regriding and the concept of “overlaps”

Fig. 4 shows various examples of overlapping IFOVs between successive instrument acquisitions, either for different spectral bands at one view angle, or of the same band acquired for different views. The overlap geometries of the individual detector-pixel footprints on ground vary significantly depending on the time differences involved and the position within the instrument swath (i.e. depending on the distance from the sub-satellite point).

In addition, the processing has to be carried out such that chunks of data (“granules”) of a configurable amount, i.e. during a configurable time of sensing, can be processed and disseminated to the end-user with high timeliness, as required by the EPS-SG overall end-user requirements (i.e., within 70 min of sensing time). Here, the lower time limit for data acquisition – during which the instrument has acquired a full sequence of multispectral and multidirectional observations for a single target on ground – has however to be respected. Taking as a reference the size of the VNIR footprint, the maximum number of views of the same target that the instrument is capable of acquiring is set to 14. Since one filter wheel turn takes 5.5 s, a set of 14 views is acquired within  $4 \times 5.5 \times 14 = 308$  s. This is the minimum input view buffer which effectively defines an area on the target coregistration grid (Fig. 5), which we call one 3MI “overlap”, and for which all the grid pixels have been seen by all spectral acquisitions, and under all observation angles (“views”). The coregistration of the measurements to the overlap generates the shortest possible level 1C data granule. Once a new instrument view is available, the set of input views is updated, and another adjacent overlap area is defined and processed.

In case the overlap area was derived simply by the footprint intersection of the 14 views of an input set (i.e. by the maximum overlap area), it would have a significant and varying overlap with the next (and previous) overlap area (Fig. 5b). Since the coregistration calculation is overall quite costly it is important to avoid processing overheads by coregistering measurements to an individual grid point twice. For this reason the actual overlap area is a subset of the maximum available overlap area and it is derived by a portion of the VNIR IFOV, so that the next overlap area is adjacent to

the proceeding one (Fig. 5c). In other words, the along track length of this portion ( $\sim 145$  km) is mainly driven by the ground speed of the satellite ( $\sim 7$  km/s) and the acquisition time of one view (22 sec). Each overlap area is therefore further reduced by processing only those pixels which have not already been processed before, or will be processed thereafter. This precalculation of the overlap area is important for an efficient implementation of the ground processing chain.

Once the overlap area for an input set of level 1B views is defined on the coregistration grid, the inverse location procedure is repeated for each grid point of this area and for all the different satellite positions for which the multi-spectral and multi-view acquisitions (i.e. those of the input set) were performed. For a given longitude and latitude of a target  $O$ , identified by the grid indexes  $J$  and  $I$ , and given all the required geometrical information as described above, the inverse location provides a mapping of  $O$  to a detector pixel  $C$  of fractional coordinates  $l_f, p_f$  (Fig. 6). For a specific spectral band and a specific viewing direction, the signal coregistered to  $O$  is then computed using bi-linear (default) or higher order interpolation of the surrounding detector pixel read-out signals  $l, p$  (provided by the level 1B product) to the fractional detector coordinates  $l_f, p_f$ . The bilinear (or bicubic) interpolation is performed for every spectral band and every angular view for which an instrument acquisition is available. The coregistration grid points are assigned to bins, into which coregistered measurements are collected.

The optimal choice for the interpolation depends on the actual instrument point-spread function (PSF) and the shape of the corresponding modulation transfer function (MTF). Since the actual PSF is not known yet, various options for different interpolation filters (bilinear or bicubic) are implemented in the L1C processor and can be selected based on the results from the instrument on-ground calibration or in-flight experience (for a discussion of the associated errors, see Section 9).

## 6. Provision of angular information

For each grid point of an overlap, the satellite and solar angle information of elevation and azimuth angle in the topocentric ref-

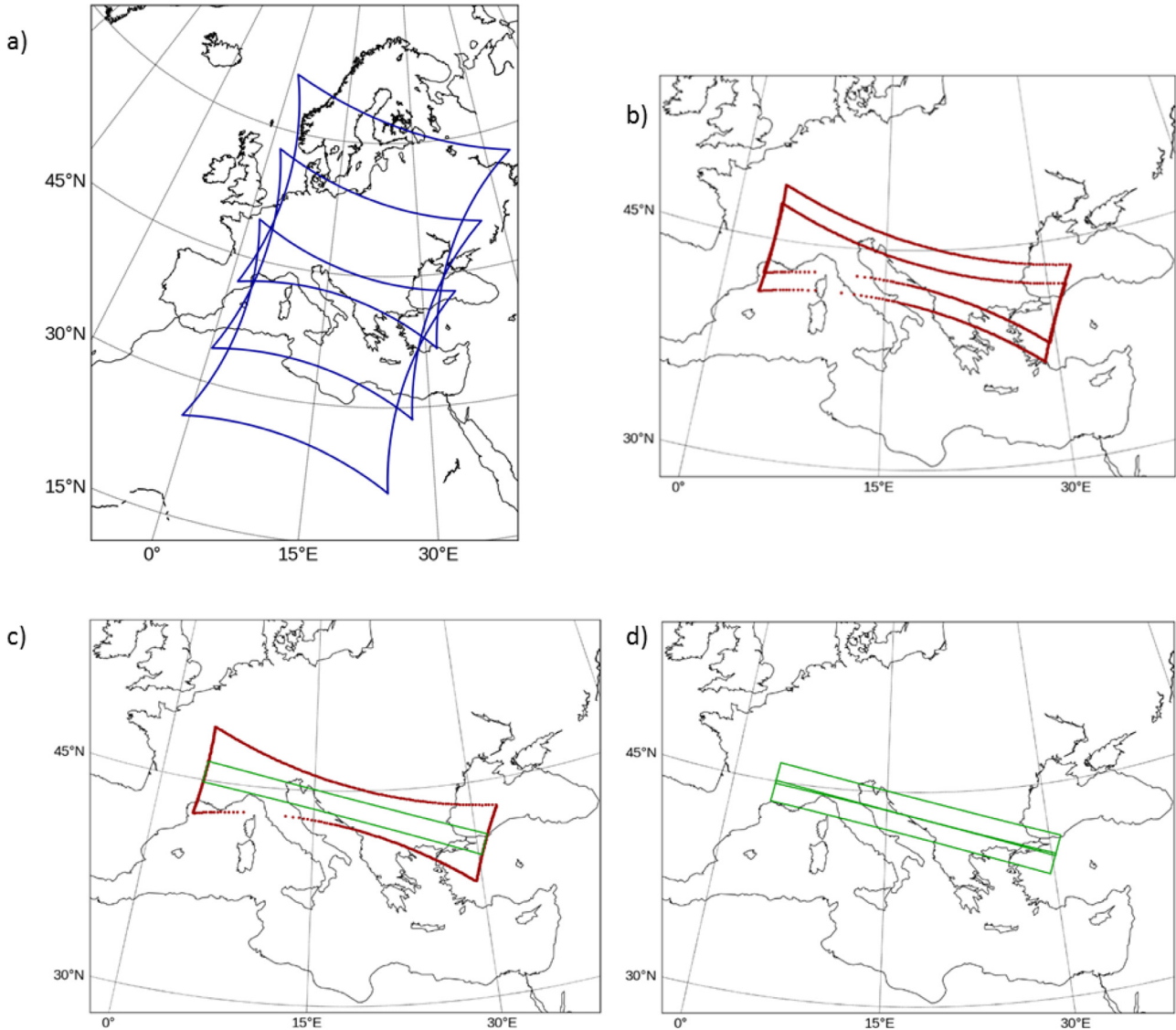


**Fig. 5.** (a) Example of a first, middle and last IFOV (view 1, 7 and 14) defining a common overlap area. b) Two consecutive maximum-intersection areas for the first 14 IFOV of a) and when removing the first view and adding the next view (view 2 to 15). c) A single maximum-overlap as in b) (red) and the common overlap area for view 1 to 14 named one “overlap” (green). It is defined such that the overlap related to view 2 to 15 is perfectly adjacent (d) and multiple processing of the same reference grid-point on ground is avoided.

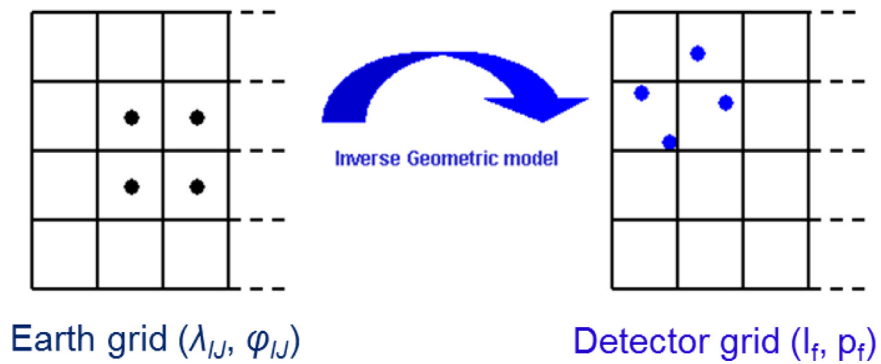


**Fig. 6.** The inverse location technique allows the coregistered measurements to be computed through a bilinear (default) or higher order interpolation of the focal plane pixels surrounding the fractional pixel determined from the inverse line of sight.

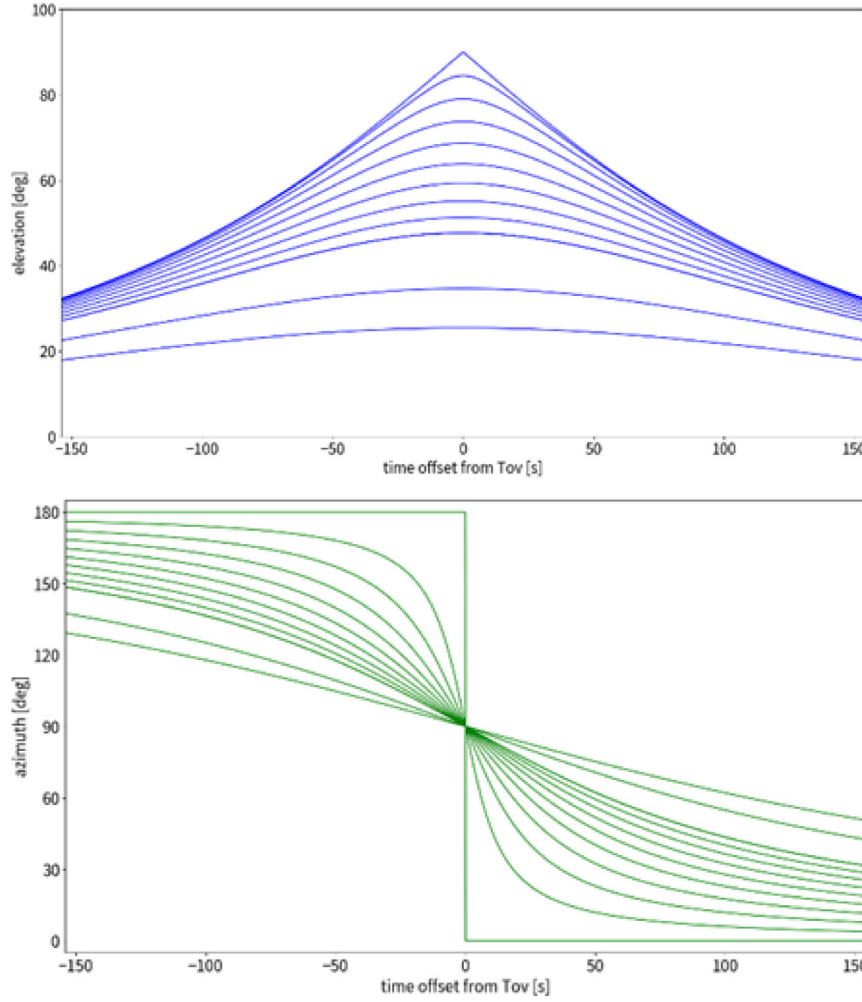


**Fig. 7.** Example of satellite elevation (top) and azimuth (bottom) angles as a function of time offset within an overlap, for different distances from the satellite ground track.

erence frame must be computed and provided for further scientific processing. For each grid point the number of angles to be provided is theoretically high with 672 angles per individual target (i.e. 4 angles for each of the 14 views and for 12 spectral bands). Encoding the full angular information would therefore significantly increase the size of the level 1C product. For this reason the absolute solar and satellite angles are provided only for the average satellite position within the 14 angular views (the average position over one wheel turn). For those users who however are interested in the exact angles relative to the single spectral acquisitions, a set of coefficients is provided for their accurate reconstruction. The fitting procedure developed yields an angular data volume reduction of up to 95% compared to encoding of the full satellite angular information.

For all grid points of one overlap, the angle fit has to cope with the motion of the Sun and the satellite during a time period of 308 s, corresponding to the sensing time of the input level 1B views. For the solar angles the problem is simple since, from the perspective of an observer on the Earth's surface, the sun position varies only very slowly in 308 s and therefore a linear fit of solar geometries is sufficient to provide accurate values of zenith and azimuth angles. The problem is more challenging for the satellite for which elevation and azimuth angles undergo rapid changes in time, mainly determined by the distance of the observer from the satellite ground track (Fig. 7).

Therefore a dedicated fitting algorithm based on a simplified orbital model has been developed for the satellite angles. The user

of the level-1C product is then provided with a small set of coefficients and a set of dedicated functions to reconstruct the elevation and azimuth satellite angles:

- Two coefficients valid for all points of the overlap area, i.e. the normalized satellite orbit radius ( $R_h$ ), the apparent angular velocity of satellite ( $\omega$ );
- Three coefficients for each point of the overlap area, i.e.: the angular ACT distance from the ground track ( $\delta$ ), the time shift to be applied to the fitting functions ( $\tau$ ), the azimuth offset ( $\phi_{\text{off}}$ );
- Two special fitting functions  $c_\theta(t)$  and  $c_\phi(t)$  for the cosine of the satellite zenith angle and for the cosine of the satellite azimuth angle, defined as:

$$c_\theta(t) = \frac{R_h \cos \delta \cos \omega t - 1}{\sqrt{R_h^2 - 2R_h \cos \delta \cos \omega t + 1}}$$

$$c_\phi(t) = \frac{\sin \omega t}{\sqrt{1 - \cos^2 \delta \cos^2 \omega t}}$$

For the reconstruction of the solar angles the following set of coefficients and equations are provided:

- Two coefficients  $m_z$ ,  $q_z$  (slope and offset) for each point of the overlap area for the linear fit of the solar zenith angle;
- Two coefficients  $m_a$ ,  $q_a$  (slope and offset) for each point of the overlap area for the linear fit of the solar azimuth angle.

**Table 3**  
Time offsets in seconds of the common and unique VNIR (V) and SWIR (S) views. Only a maximum of 12 views of the SWIR band can be coregistered to one target because of the smaller detector layout. Depending on the position over the orbit the SWIR views range from view idx 3 to 14 up to 6 to 17.

view idx ( $v$ )	0	1	2	3	4	5	6	7	8	9	0	11	12	13	14	15	16	17	18	19	20
Optical head	V	V	V	V/S	S	V/S	S	V/S	S	V/S	S	V/S	S	V/S	S	V/S	S	V/S	V	V	V
Time offs $\Delta t_v$	-143	-121	-99	-77	-66	-55	-44	-33	-22	-11	0	11	22	33	44	55	66	77	99	121	143

**Table 4**  
Time offsets in seconds of the single spectral bands acquired during a single VNIR/SWIR view (see also Table 1 and [12]).

band idx ( $k$ )	0	1	2	3	4	5	6	7	8	9	10	11
W1	VNIR 410	VNIR 443	VNIR 490	VNIR 555	VNIR 670	VNIR 763	VNIR 765	VNIR 865	VNIR 910	SWIR 1370	SWIR 1650	SWIR 2130
Time offs $\Delta t_k$	-0.75	+0.75	-2.25	-1.5	0	+2.0	+2.5	+1.5	+2.25	-1.5	+1.5	0

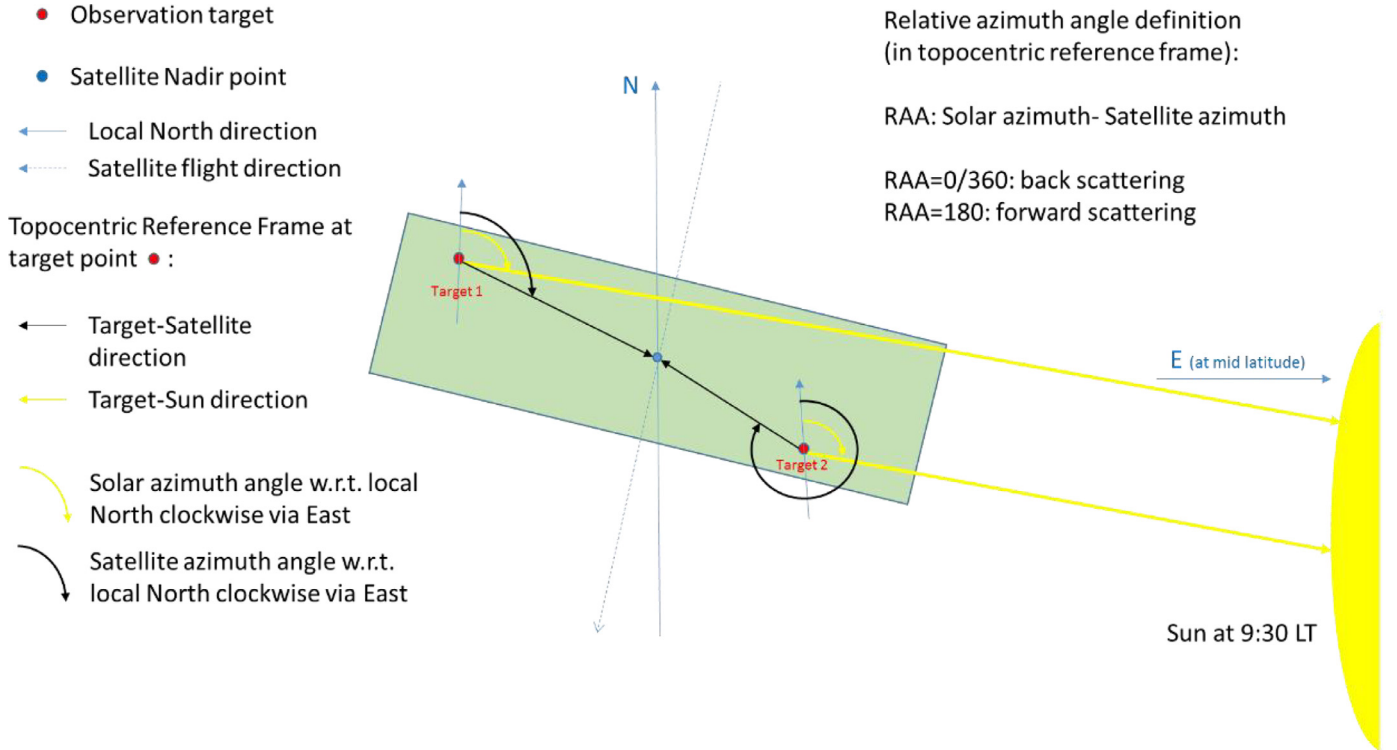


**Fig. 8.** Topocentric Earth reference frame used for the 3MI level 1C and higher products. Angles are defined with respect to North and counted clock-wise. The green shaded area illustrates one overlap of the level-1C product. Red dots: 2 different viewing geometry target points on the grid are illustrated, one in backscattering geometry (target 1) and the other in forward scattering geometry (target 2).

The complete angle reconstruction functions for the time varying satellite zenith and azimuth angles are:

$$\theta_{\text{sat}}(t) = \cos^{-1}[c_{\theta}(t - \tau)],$$

$$\phi_{\text{sat}}(t) = \phi_{\text{off}} + \text{sgn}(\delta) \cdot \cos^{-1}[c_{\phi}(t - \tau)],$$

and for the Sun:

$$\theta_{\text{sun}}(t) = m_z t + q_z,$$

$$\phi_{\text{sun}}(t) = m_a t + q_a.$$

In this way the angles can be reconstructed for each grid point at a specific time offset  $t_{\text{off}}$ , depending on the spectral band and view of interest. Tables 3 and 4 report the spectral band ( $\Delta t_k$ ) and view ( $\Delta t_v$ ) offsets for the case in which 14 VNIR and 12 SWIR views are coregistered to the output overlap area. For a specific spectral band of a specific view the sampling time offset  $t^{v,k}$  is then calculated as:

$$t_{\text{off}}^{v,k} = \Delta t_v + \Delta t_k.$$

For example, if the satellite angles have to be derived for VNIR band at 765 nm for view 12, then the fitting functions will be evaluated at  $t_{\text{off}} = 22 + 2.5 = 24.5$  seconds.

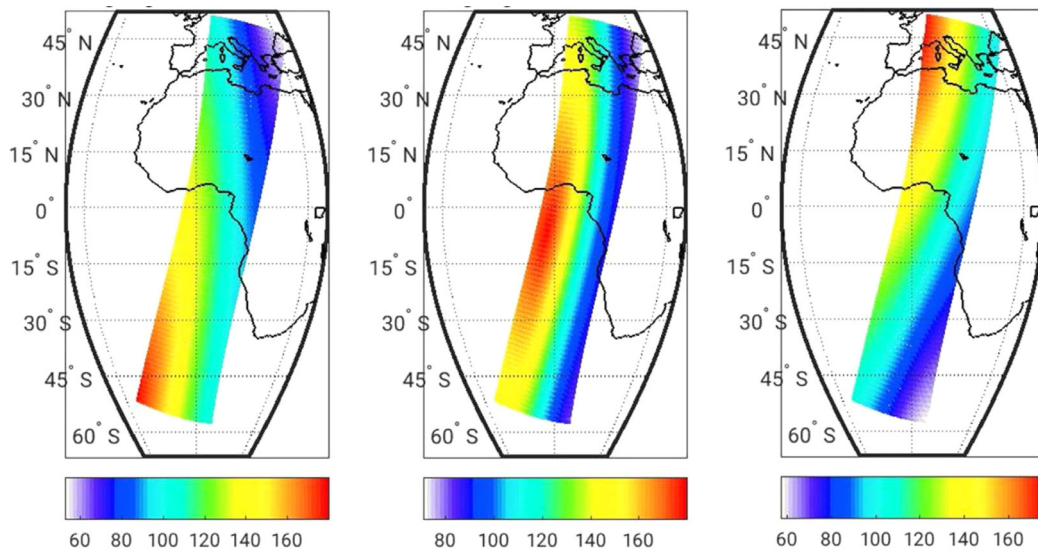
For every angular value reconstructed with this algorithm, a check on the result should be performed in order to make sure that the angle falls in the range  $0^\circ$ – $360^\circ$  (otherwise  $360^\circ$  need to be subtracted). For details on the derivation of the angular equations we refer to [9].

Fig. 8 shows the definitions of the azimuth and relative azimuth angles as applied for 3MI processing.

Within this convention, the scattering angle is  $0^\circ$  for backward scattering and  $180^\circ$  for forward scattering of light towards the instrument and calculated as:

$$\Theta = \cos^{-1}[\sin \theta_{\text{sun}} \sin \theta_{\text{sat}} \cos[180 - (\phi_{\text{sun}} - \phi_{\text{sat}})] - \cos \theta_{\text{sun}} \cos \theta_{\text{sat}}].$$

Fig. 9 shows the scattering angle over the daylight part of one orbit of the EPS-SG platform for view 1, 7 and 14 of the VNIR detector. Fig. 10 shows the minimum, maximum scattering angle



**Fig. 9.** Scattering angle as calculated for the solar and satellite zenith and azimuth angles from the L1C product for one simulated EPS-SG orbit (daylight side  $\text{SZA} < 75^\circ$  only). The scattering angle is shown for VNIR view 1, 7 and 14 left to right.

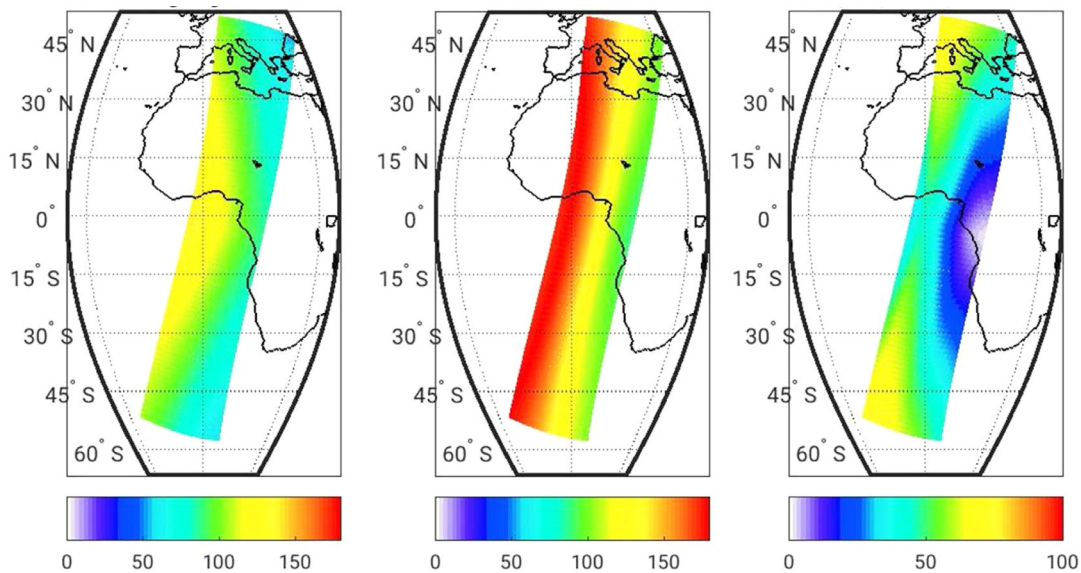


**Fig. 10.** The scattering angle minimum (left panel), maximum (middle panel) and its range (right panel) as derived from all 14 VNIR views per fixed-grid point for the daylight side ( $\text{SZA} < 75^\circ$ ) of one EPS-SG orbit.

and its range for each position over this orbit for the VNIR channels. Note that the scattering angle range covered by 3MI measurements for each location over the orbit varies significantly and is very narrow in the eastern equatorial region. The scattering angle range and its orbital pattern are very different between a morning orbit (9:30 LT) for EPS-SG and a mid-day orbit e.g. for PARASOL. Fig. 11 shows the SWIR detector observation geometry for views corresponding to the VNIR views 5, 7 and 10. Fig. 12 shows the corresponding SWIR channels minimum, maximum scattering angle and its range for each position over the orbit.

## 7. Colocation of ancillary data

The L1C processor contains a generic colocation module, which can colocate ancillary information provided at similar or larger spatial resolution, or at significantly higher spatial resolution. In case the ancillary data provided is of similar or higher spatial resolution the colocation method of choice is a polygon-polygon in-

tersection method, for which the 3MI pixels are represented by a polygon of 4 vertices around the centre location (provided by the level-1B product) and the ancillary data by a polygon with  $n$ -vertices depending on the footprint characterisation (e.g. an ellipsoid footprint would be represented by 8 vertices as a best compromise for accuracy and processing cost). Detector pixel polygons projected on the earth surface (or the geoid) have significantly different shapes and span different areas depending on how close they are located to the sub-satellite point (see grey and black subset of pixel projections in Fig. 13).

For the 3MI level-1C product the most important colocation is however the colocation with METimage observations provided at a significantly higher spatial sampling (500m) than the one of 3MI. In this case the colocation method of choice is a point in polygon collection of METimage data, where each METimage measurement is treated as a dimensionless point measurement and a set of measurements is identified within one 3MI observation (Fig. 13). Binary cloud-flag information from METimage (cloudy/non-cloudy

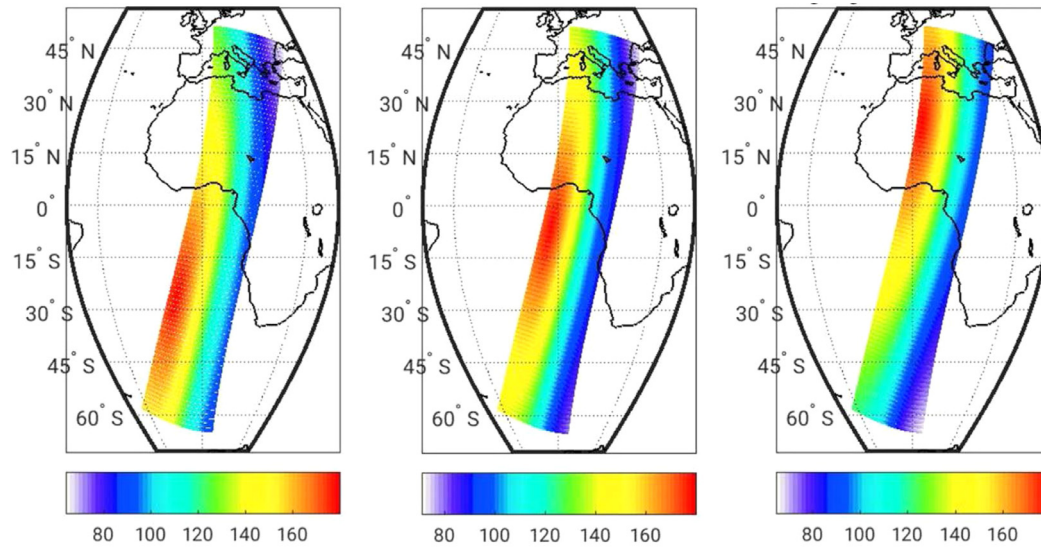


Fig. 11. Same as Fig. 9 but for the SWIR channels and for observations corresponding to VNIR view 5, 7 and 10.

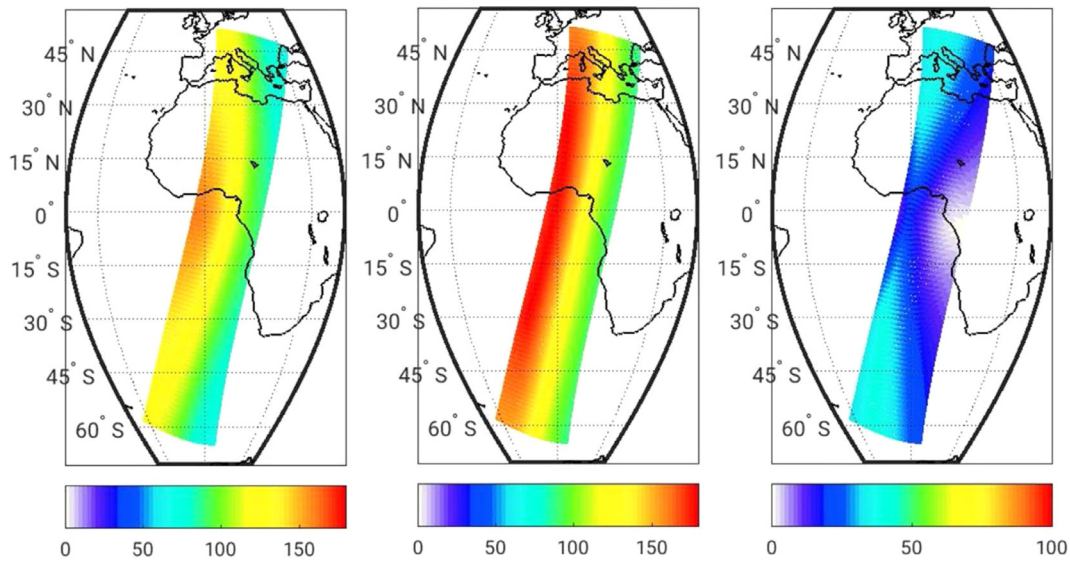


Fig. 12. Same as Fig. 10 but for the SWIR channels scattering angle minimum (left panel), maximum (middle panel) and its range (right panel).

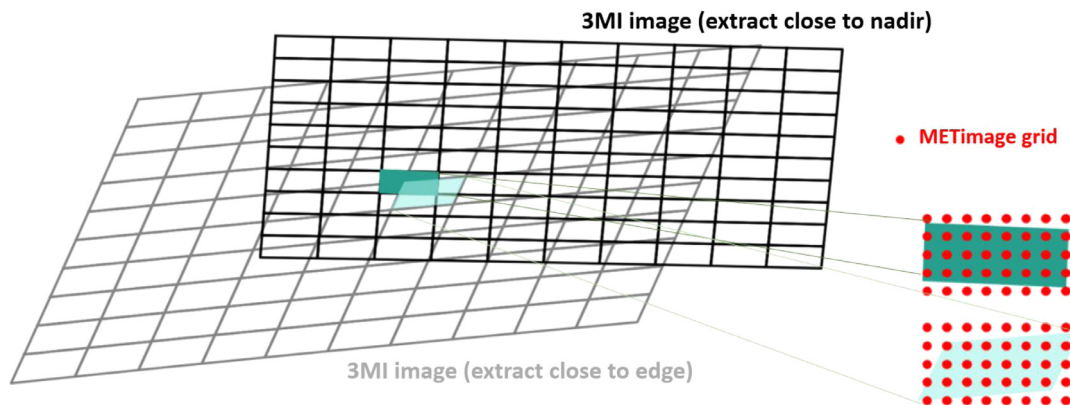
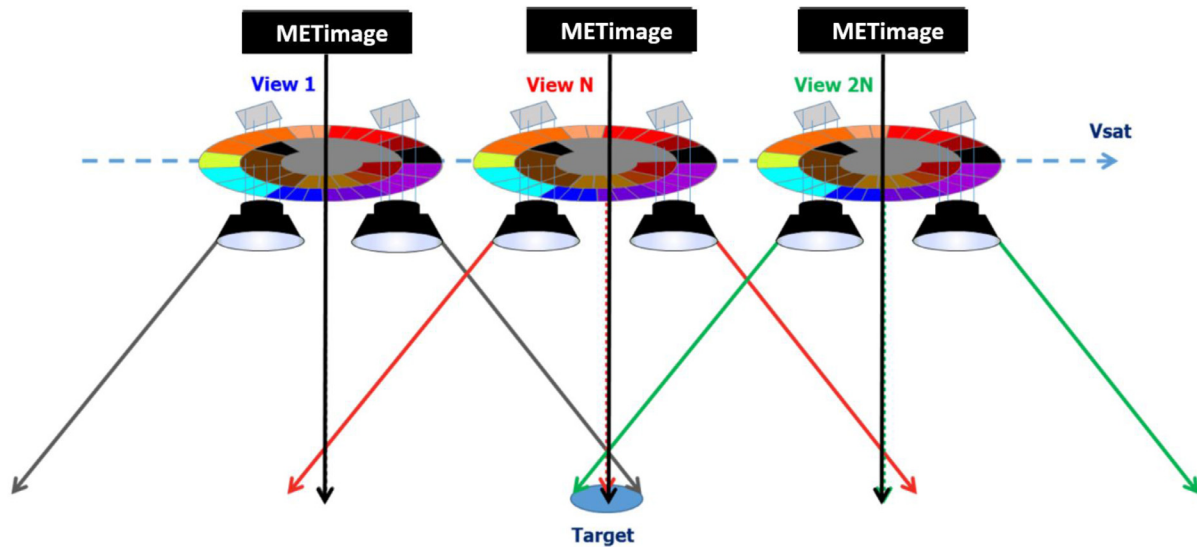
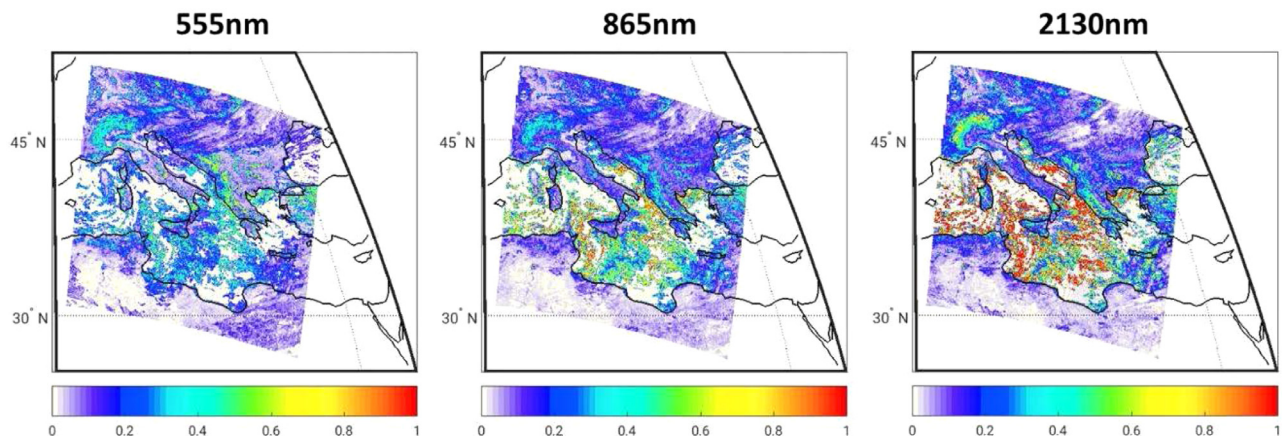


Fig. 13. 3MI footprints for colocation with ancillary data are represented as polygons with 4 vertices around the centre pixel location (provided by the level-1B processing). The grey and black polygons show a small subset of pixels of the IFOV close to the Nadir point (black) and towards one edge of the IFOV (grey). Here we present the case for a point in polygon colocation approach (see inset at the bottom), which is predominantly used in the L1C processor for colocation of METImage observations taken at significantly higher sampling (500m) and treated as dimensionless points. Depending on the 3MI observation geometry, the projection of the detector pixel polygon on ground can cover quite different areas (lower right side), which then affect the selection of associated METImage point observations and therefore the aggregated METImage ancillary data result.



**Fig. 14.** Simultaneous METImage observations are available for the 3MI Nadir full swath only. As a consequence colocated METImage information, like cloud-fraction, CTH and scene-inhomogeneity for targets observed under off-Nadir geometry exhibit a temporal observation difference of up to 159 s plus a difference in observation geometry.



**Fig. 15.** Scene inhomogeneity as derived from colocated METImage radiance measurements and re-gridded to the target fixed grid of the 3MI level 1C product. Low values indicate very homogeneous scenes and high values very in-homogeneous scenes from METImage normalised radiance standard deviations at 555, 865 and 2130 nm (left to right).

pixel information) can then be aggregated to a geometrical cloud-fraction (CFR) associated with one 3MI pixel, and additional ancillary information (like cloud-top height (CTH) or radiances) can be provided as geometric mean or standard deviation values.

However, simultaneous observation of METImage with a similar observation geometry is only available for the Nadir part of the 3MI full swath (Fig. 14). The time difference between the same target observed by METImage and 3MI at the largest observation angles is  $\pm 159$  sec and the difference in observation angle further reduces the observed signal response correlation. Therefore the level-1C product also provides a simpler collocation of METImage and surface properties (snow/ice and land fraction) collocated directly to the target pixel.

METImage's subpixel information is provided in the EPS-SG ground segment to the L1C processing chain by an intermediate "fast-track" L2 product dedicated to the 3MI L1 and L2 processing chain. This intermediate product provides a cloudy or non-cloudy pixel flag and a CTH estimate. The METImage CTH used here is part of the "fast-track" operational pre-processing of cloud information in the METImage level-2 operational processing chain. The CTH retrieval algorithm uses the visible imaging of METImage in the oxygen A-band [2,10]. The L1C processing in addition receives radiance

fields from three channels of METImage: 555, 865 and 2130 nm. From the point-in-polygon collection of signals, both from the "native" grid-pixel collocation and the "direct" collocation to the fixed registration-grid, the L1C processor produces a 3MI pixel averaged quantity using cloud-mask, CTH, and radiance information from METImage, in order to provide cloud-fraction, average CTH, and scene-inhomogeneity for the individual 3MI pixel and as shown in Fig. 15. The latter is calculated as

$$Inh = \frac{\sigma}{\bar{I}} \Big]_{\lambda_{MET}}$$

where  $\sigma$  is the standard deviation of the radiance field  $I$  as observed by METImage within a 3MI pixel for all three METImage wavelengths  $\lambda_{MET}$  provided and  $\bar{I}$  is the mean over these radiances. In principle the width of the 3MI PSF can be taken into account in any such collocation and averaging process. However, since the shape of the instrument PSF is not known yet, here the PSF is assumed to have a boxcar shape with a width equal to the spatial sampling distance.

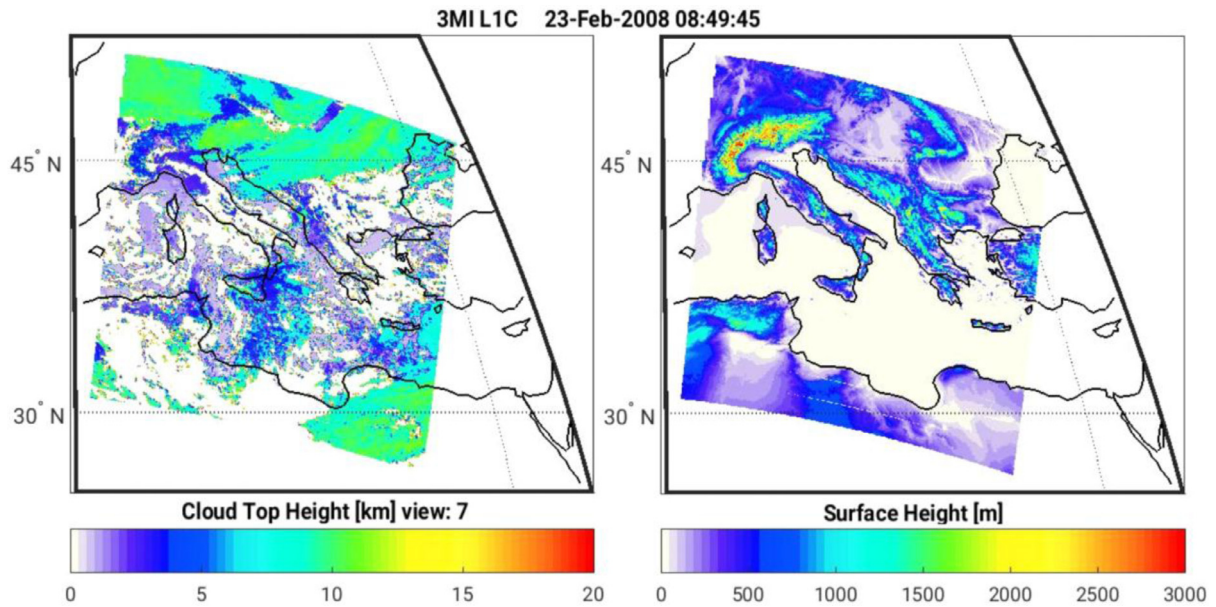


**Fig. 16.** Left: Colocated METImage CTH as provided in the L1C product and used for parallax correction in case the cloud contribution to the signal is more than 50%. Right: surface height as geometric mean per detector pixel taken from the ACE2 static digital elevation model [1].

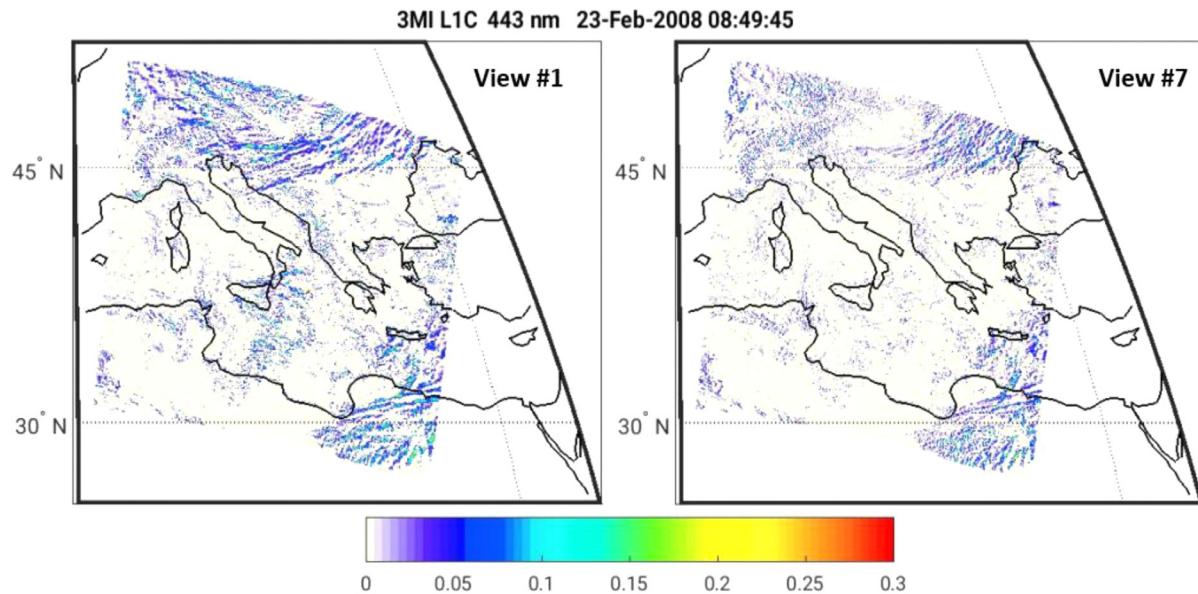


**Fig. 17.** Absolute differences between parallax corrected and non-parallax corrected reflectance factor values for the 443 nm channel, for view 1 (left) and 7 (right).

## 8. Parallax correction

As introduced in Section 4, the “parallax correction” comes at no additional cost with the inverse pointing coregistration method. The distance from the earth centre  $R+P$  (or the centre of the polar coordinate system; see Fig. 3) is already required to be calculated, also in the case where the observer is situated at the geoid ( $P=0$ ). Here we consider three different cases for processing:  $P=0$  (geoid: “no parallax correction”),  $P$ =surface (using a digital elevation model (DEM): “parallax correction to DEM”), and  $P$ =CTH (“parallax correction to cloud-top height”).

Parallax correction to the DEM and to the geoid is straight forward since  $R+P$  is provided by a static relation or DEM database. For the choice of a parallax correction where  $P$ =CTH the L1C processing implements the following algorithm. Since CTH information is also available at subpixel scale from colocated METImage

CTH information, we investigate for any target  $O$  the relative radiance contribution from the surface and from the cloud top. This is done by co-locating all METImage radiance values inside the 3MI detector-pixel footprint around target  $O$ , assigning them using the associated METImage cloud-mask to a cloud-free or cloudy bin, then calculating from each bin total integrated cloud-free and cloudy radiance values. A decision on the “dominant signal” is then made based on the total integrated radiance coming from cloudy or from non-cloudy pixels. Currently the separation is made at the 50% threshold. This means that in case the integrated radiance of the cloudy METImage observations is larger than the integrated radiance of the non-cloudy ones, the parallax correction is carried out according to the CTH of the cloudy pixels. If the signal of the clear pixels dominates, the parallax correction is carried out according to the averaged surface elevation as obtained from the DEM for the clear pixels.

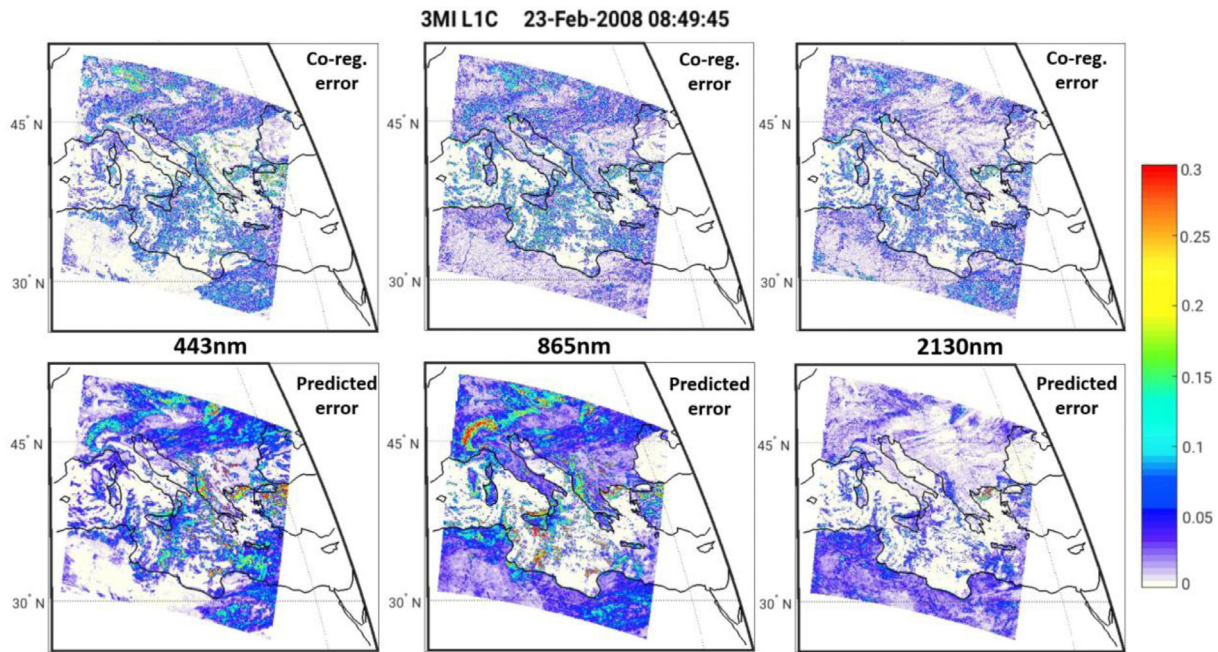


**Fig. 18.** Top-panels: Coregistration error derived as residual between coregistered L1C reflectance factor values and a simulated “perfect” L1C dataset for channel 443, 865 and 2130 nm (left to right column) and for view 1. Lower panels: The predicted L1C error based on collocated METImage scene-inhomogeneity data (see Fig. 15) for the same channel and view.

Fig. 16 shows an example of DEM and CTH data collocated to the coregistration grid and Fig. 17 shows the differences between parallax corrected and non-parallax corrected reflectance factor values for two distinct views of the 443 nm channel.

The CTH provided by a METImage “fast” and intermediate processing dedicated for 3MI L1C processing in the EPS-SG ground segment is retrieved using oxygen A-band absorption measurements from the METImage channels. The CTH is therefore sensitive to the optically thicker case, in case of multi-layer clouds, and therefore is more representative of an averaged mean scatter height instead of the maximum geometrical CTH for any given scene.

### 9. Estimate of the radiometric error due to spatial aliasing and regridding

The overall radiometric error of the coregistered and resampled radiances provided in the L1C product consist of four components:

- 1) The instrument noise;
- 2) The uncertainty in the instrument absolute radiometric knowledge;
- 3) The uncertainty knowledge of the observation geometry per acquisition. This uncertainty has three components:
  - a the pointing error of the instrument,
  - b the position error of the satellite, and
  - c the error of the inverse geometrical model (using EO-CFI).
- 4) The error introduced by spatial aliasing and the associated interpolation method when regridding the data towards the target.

All of these error components impact directly or indirectly the radiometry at level-1C, especially when the target fixed grid area is not spatially homogeneous.

Note that the L1C product will however not attempt to provide an error estimate of the absolute radiance accuracy and of any biases introduced by deficiencies in the accurate knowledge of the instrument calibration (both on-ground and in-flight) – point 2) and 3). The absolute product accuracy (like the accuracy of the

pointing knowledge) will be subject to extensive validation campaigns during commissioning and to the continuous monitoring and validation efforts carried out during the operational phase of the mission at EUMETSAT based on the experience from in-orbit vicarious calibration methods applied to PARASOL [11]. Instead the L1C product will provide an estimate of those contributors to the radiometric error which can be used (e.g. in sub-sequent retrievals of geo-physical parameters) as randomly distributed errors (point 1). The instrument noise component  $\sigma$  is provided by the L1B product as input to the L1C processing. In the following we will then provide a way to estimate the introduced error by spatial aliasing (essentially the insufficient sampling or under-sampling of the PSF) and regridding (interpolation; point 4), using the subpixel inhomogeneity information provided by METImage (see above). The spatial aliasing error is derived such that it can be used as an additional noise component added to the instrument detector noise and used within e.g. a data-assimilation system. The overall random error of the radiances at L1C provided in the product is then given by

$$R_{\text{err}} = \sqrt{E^2 + \sigma^2}$$

where  $E$  is the random error contribution due to spatial aliasing and regridding provided for all derived Stokes vector components.

The overall coregistration and regridding error results from signal interpolation of all detector pixel read-outs surrounding the fractional detector pixels associated with the target point  $O$  (see Fig. 3) and the spatial aliasing (due to under-sampling) of the instrument detector signal sampling at spatial frequencies above Nyquist frequency. The associated signal error  $E$  then depends on the interpolation method, the shape of PSF of the instrument, and on the projected signals. In case the resulting MTF has a considerable amount of the total energy associated with frequencies above the Nyquist-frequency, those spatial frequencies will result in an incorrect transfer of information during the interpolation, also known as spatial aliasing. This error is unavoidable in case any regridding of the native instrument grid is carried out, and is a function of the instrument spatial resolution and the observed spatial frequencies. The error due to spatial aliasing therefore does

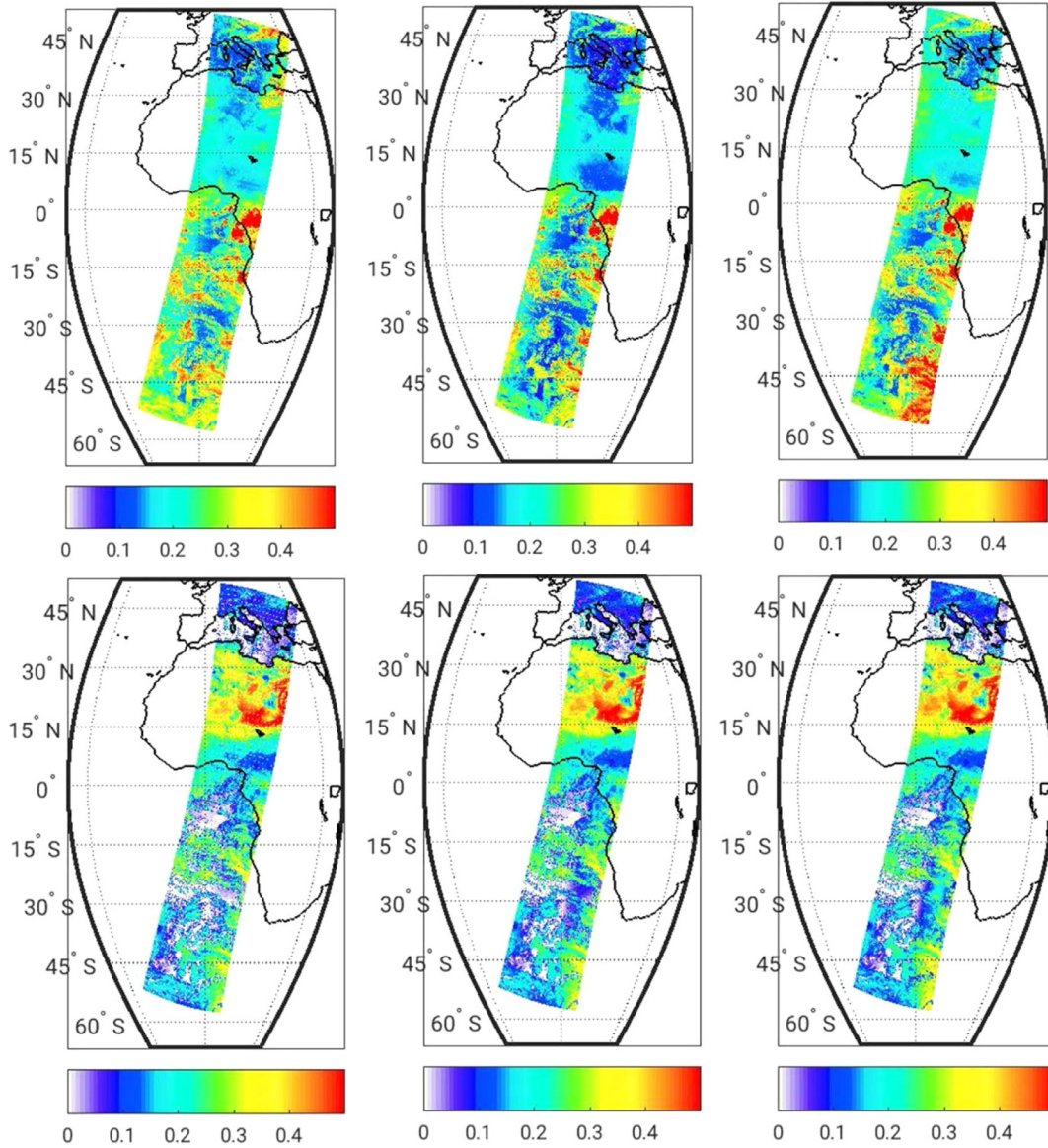


**Fig. 19.** Top row: Reflectance factor values for I and for the same viewing geometries as presented in Fig. 9 from left to right for the 443 nm VNIR channel (view 1, 7, 14). Bottom row: Same as top row but for the 2130 nm channel of the SWIR detector.

not depend on the applied coregistration strategy (apart from the choice of the 2D interpolation method). For instruments with PSFs of Gaussian shape and a proper oversampling by the instrument of its spatial resolution the error is negligible. However, this can only be achieved by optics with significantly lower spatial resolution than the spatial sampling of the detector (so for 3MI this would mean an optics with a significantly lower resolution than 4 km). At the same time the dynamic range of the signal-to-noise response of the instruments may suffer, since less total energy is focused on one detector pixel for the purely Gaussian, oversampled case. Therefore a trade-off has to be found between a low spatial resolution and high oversampling on the one hand and high spatial resolution and low oversampling on the other hand. The former is associated with low and the latter with high radiometric coregistration errors and also, due to the low over-sampling, a large dynamic range of the instrument response i.e. the case for which the PSF would have a perfect “boxcar” shape (which is essentially the case for the level-B TOA test dataset used as input for this study).

Since the error associated with spatial aliasing for any interpolation strategy is predominantly a function of the observed spa-

tial frequencies for any given PSF shape we will use the standard deviation  $\sigma_{I_{JJ},MET}$  of the radiances co-located from METimage (i.e. the previously derived inhomogeneity times the average METimage radiance  $I$  over the fixed-grid pixel) within the 3MI coregistration pixel and surrounding pixels, multiplied with the square of the sine of the scattering angle  $\theta$ ,

$$E(p_i) = Z_{MET}(p_i) \sin^2(\theta),$$

in order to provide a radiometric error estimate  $E$  in dependence of a set of empirical parameters  $p_i$  associated with the coregistration step. The following calculations are performed separately and in the same way for each Stokes vector component  $I$ ,  $Q$ , and  $U$ . Therefore we drop the Stokes vector dimension for clarity.  $Z_{MET}$  is the result of a linear combination of  $i=0, \dots, n$  aggregates of subpixel scene radiance standard deviations at the target  $O$  ( $i=0$ ) and for surrounding pixels of distance  $i=1, \dots, n$  (in fixed-grid pixel space) with weights  $p_i$ , such that:

$$Z_{MET}(p_i) = p_0 S_{OV} + p_1 \begin{pmatrix} 0 & 1 & 0 \\ 1 & 0 & 1 \\ 0 & 1 & 0 \end{pmatrix} * S_{OV} + p_2 \begin{pmatrix} 1 & 1 & 1 \\ 1 & 0 & 1 \\ 1 & 1 & 1 \end{pmatrix} * S_{OV}$$

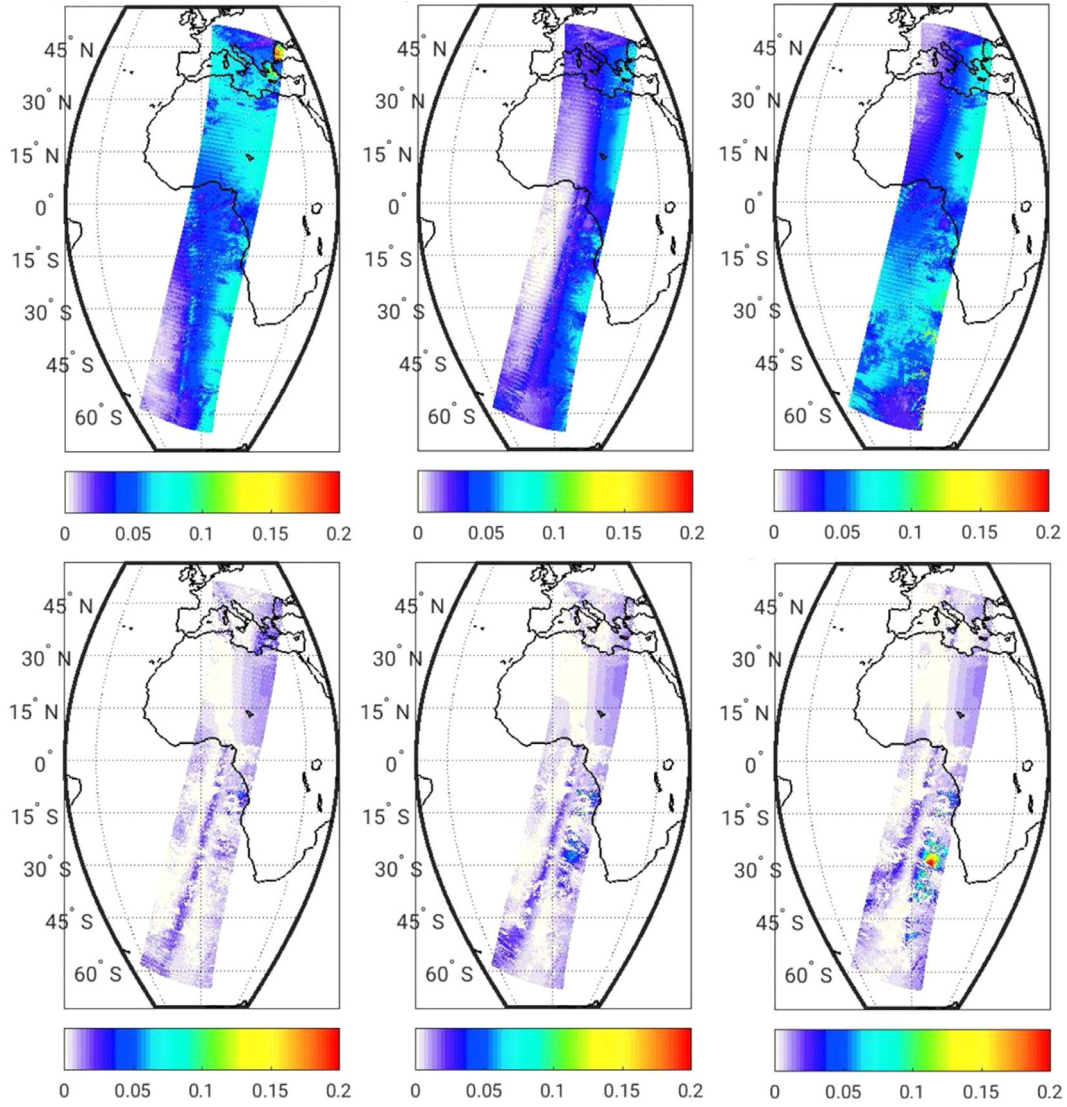


Fig. 20. Same as Fig. 19 but for the polarised reflectance factors P.

$$+ p_3 \begin{pmatrix} 0 & 0 & 1 & 0 & 0 \\ 0 & 1 & 0 & 1 & 0 \\ 1 & 0 & 0 & 0 & 1 \\ 0 & 1 & 0 & 1 & 0 \\ 0 & 0 & 1 & 0 & 0 \end{pmatrix} * S_{OV} + \dots$$

Here  $S_{OV}$  is the matrix of all standard deviation values  $\sigma_{IJ,MET}$  collocated for all fixed grid pixels of the current overlap. In this way the resulting matrix from each order of convolution provides a matrix associated with  $O$  at the fixed-grid point  $IJ$  for all observed METimage radiance standard deviations at pixel distance  $i=0, \dots, n$ . For a 2D bilinear interpolation, only detector pixels of up to  $i=1$  pixel distance and their associated subpixel  $\sigma_{IJ,MET}$  contribute to the interpolation error, while in case of e.g. cubic 2D interpolation methods higher orders of  $i$  may play a role. The linear regression coefficients  $p_i$  are then found using a test-dataset of realistic radiance (and subpixel inhomogeneity) fields and by comparing the coregistered radiances with a “perfect” L1C dataset, for which the TOA radiances are calculated directly on the coregistration fixed-grid and are not interpolated from the instrument native ground pixel grid (i.e. no regridding error is involved for the “perfect” L1C product). From this perfect L1C we then derive a reference dataset of absolute and normalised radiometric errors

$E_{L1CPerfect}$  with  $E_{L1CPerfect} = |R_{L1Cperfect} - R_{L1C}|$ , and subsequently the coefficients  $p_i$  by minimizing:

$$\min_i |E_{L1Cperfect} + \ln(1 - E(p_i))|.$$

The results for  $p_i$  for all channels and views (as well as for  $I, Q, U$ ) are then stored separately. This look-up table (LUT) of coefficients  $p_i$  (in the bi-linear case there are only two coefficients per observation) can then be used to derive an associated coregistration error  $E(p_i)$  for any given scene at very low computational cost and from the available scene-inhomogeneity information  $Z_{MET}(p_i)$  (including the surrounding pixel inhomogeneity information), the coregistered radiance field, and the scattering angle. The processing is done after the processing of each overlap and the associated radiometric error is reported in the L1C product accordingly.

Fig. 18 shows the absolute difference in reflectance  $E_{L1CPerfect}$  when comparing the coregistered results from the 3MI L1C processing output  $R_{L1C}$  (starting from individual 3MI L1B calibrated images) to the TOA reflectance factor values forward modelled starting directly from the fixed coregistration grid  $R_{L1Cperfect}$ , as well as the corresponding predicted error  $E(p_i)$ . Results are shown for view 7 and for 443, 865 and 2130 nm. The METimage scene standard deviation values  $\sigma_{IJ,MET}$  are taken from the collocated radiances of the METimage 555, 865 and 2130 nm bands as shown

in Fig. 14. Note that due to operational processing constraints the radiance values of only three METimage bands (555, 865 and 2130 nm) can be made available for L1C processing. The error prediction of any given coregistered 3MI band will make use of the one out of three METimage bands, which is spectrally closest.

The predicted error  $E(p_i)$  represents the true radiometric error  $E_{L1CPerfect}$  quite well on average, but as can be expected, it is generally not able to capture all small scale variations in the true  $E_{L1CPerfect}$ . In general we consider the performance of the error prediction satisfactory, especially when considering that such an estimate was not available for similar products in the past (because of the lack of very precisely collocated and simultaneously measured subpixel scale information).

For the TOA reflectance TDS used here no PSF has been applied, also since the actual shape of the PSF of the 3MI instrument is currently not known. Without a realistic PSF applied to the TDS provided for the 3MI native instrument grid, the results presented here can be considered as a worst-case scenario for the associated coregistration error, since no PSF essentially means a “perfect” box-car with a very high MTF component of frequencies above Nyquist (and therefore significant spatial aliasing). To the best of our current knowledge regarding the current instruments optical design the actual PSF of 3MI will be much more Gaussian like and therefore the coregistration errors are expected to be smaller than those presented here.

## 10. Results

Finally, we present some selected examples of coregistered and collocated reflectance factor values, as provided in the L1C product.

Fig. 19 shows reflectance factor values for simulated top-of-atmosphere radiance values  $I$  for the same orbit and therefore for the same collocated observation geometries as presented in Fig. 9 for the 443 nm of the VNIR detector (top row) and for the observation geometries as presented in Fig. 11 for the 2130 nm channel of the SWIR detector (bottom row).

Fig. 20 shows the corresponding polarised reflectance factors  $P$  for the same orbit, channels and observation geometries.

## 11. Conclusion and product dissemination

The Multi-viewing Multi-channel Multi-polarisation Imager (3MI), to be flown as part of EPS-SG, will provide the capability to measure microphysical properties of aerosol, clouds and surface properties with an unprecedented number of independent pieces of information relating to the large parameter space of these target variables. Continuing from the multi-angle, polarised measurement capabilities of the POLDER instruments, 3MI will provide an extended spectral range covering the shortwave infra-red region, with additional polarisation measurements in the visible and near-infrared region. With an expected launch of the first of the three EPS-SG platforms in 2022, and a projected mission lifetime per instrument of about 7 years, 3MI will monitor the impact of aerosol and clouds on atmospheric composition and climate change into the 2040s. 3MI data products will make use of the large capabilities of other instruments on the EPS-SG satellites, most notably the cross-track scanning imaging spectroradiometer METimage measuring between 0.443 and 13.345  $\mu\text{m}$  at a spatial sampling of 500 m and thus providing valuable additional subpixel scale information on scene homogeneity and cloud properties.

In order to provide to users of 3MI level-1 data a well calibrated, easy to use dataset, the EUMETSAT operational level 1C processor will geoproject and regrid the measured Stokes vector radiances  $I$ ,  $Q$ , and  $U$  for all angles and for all spectral bands observed, to each point on a fixed earth surface grid of 4 km resolution achieving global coverage within one day below 70° latitude. The products will be disseminated in granules of data not

more than 1.5 h after sensing and each granule of data will contain one or more sub-regions of the global fixed grid which are called “overlaps”, observed by 3MI for 14 observation geometries during ~5 min of sensing. The level-1C product granules will be disseminated in NetCDF and the parameter tree is organised such that the individual overlaps contained in the product are easy to merge to cover a larger part or even the full earth fixed-grid.

The product contains valuable ancillary cloud property information, such as cloud-top height and cloud fraction, along with three values for subpixel scene homogeneity at 555, 865 and 2130 nm, collocated and aggregated from the METimage measurements, with a temporal correlation of less than 2.5 min. In addition land-surface fraction, elevation and snow-ice fraction are also provided.

Observation geometries are provided in a condensed way for all spectral channel and viewing angles, by using a set of coefficients to reconstruct the large amount of angular data with a high precision. In addition, in case such precision is not needed, the angles associated with the centre wheel position time and for all views are provided as absolute values.

Radiance values are provided separately for the  $I$ ,  $Q$  and  $U$  components of the Stokes vector for all polarised channels except, 763, 763, and 910 for which only  $I$  is provided. Radiances are represented as reflectance factor values normalised by the band integrated solar irradiance times  $\pi$  and corrected for the seasonal sun-Earth distance variation. The solar constant values are provided separately per channel for reconstruction of radiances if needed.

All re-projected radiances are parallax corrected either to the surface height or to the collocated averaged cloud-top height as provided by METimage, depending on whether the dominant part of the observed signal is coming from the surface or from the cloud-top. Again, the latter contribution is evaluated from the METimage subpixel scale radiances collocated to the 3MI level-1C fixed-grid.

Finally radiometric random errors are provided composed of the random noise detector component and the random component introduced by the regridding of the radiance fields to the fixed grid. This latter component is derived from the associated scene-inhomogeneity as observed by METimage and transferred to a subpixel homogeneity, which is empirically correlated to the introduced regridding error. In such a way we provide a radiometric error component which should be useful for model assimilation or in optimal estimation or similar retrieval schemes relying on observation vector covariance fields of a reasonably Gaussian nature. The error introduced by geoprojection turns out, in contrast to be sufficiently small in order to be neglected.

By providing this kind of geoprojected and re-gridded 3MI level-1 dataset with the associated ancillary information we hope to make a significant long-term contribution to the monitoring of the aerosol and cloud microphysical properties and their role in the Earth atmospheric composition and climate.

## Supplementary materials

Supplementary material associated with this article can be found, in the online version, at doi: [10.1016/j.jqsrt.2018.12.022](https://doi.org/10.1016/j.jqsrt.2018.12.022).

## References

- [1] Berry PAM, Smith RG, Benveniste J. ACE2: the New Global digital elevation model. In: Mertikas S, editor. Gravity, geoid and earth Observation. International association of geodesy symposia, 135. Berlin, Heidelberg: Springer; 2010. p. 231–8. ISBN: 978-3-642-10633-0.
- [2] Compiègne M, C-Labonnote L, Dubuisson P, Ferlay N, Ramon D, Riedi J. Cloud top pressure retrieval from O2 A-band with MET image. In: EUMETSAT Meteorological Satellite Conference; 2015. p. 21–5. September.
- [3] Deschamps YP, Breon F-M, Leroy M, Podaire A, Bricaud A, Buriez J-C, Seze G. The POLDER mission: instrument characteristics and scientific objectives. Geoscience and remote sensing. IEEE Trans 1994;32:598–615. doi:10.1109/36.297978.

- [4] Diner DJ, Boland SW, Brauer M, Bruegge C, Burke KA, Chipman R, Girolamo LDi, Garay MJ, Hasheminassab S, Hyer E, Jerrett M, Jovanovic V, Kalashnikova OV, Liu Y, Lyapustin AI, Martin RV, Nastan A, Ostro BD, Ritz B, Schwartz J, Wang J, Xu F. Advances in multiangle satellite remote sensing of speciated airborne particulate matter and association with adverse health effects: from MISR to MAIA. *J Appl Remote Sens* 2018;12(4):042603. doi:10.1117/1.JRS.12.042603.
- [5] Dubovik O, Li Z, Mishchenko MI, Tancré D, Karol Y, Bojkov B, Cairns B, Diner DJ, Reed Espinosa W, Goloub P, Gu X, Hasekamp O, Hong J, Hou W, Knobel-spiess KD, Landgraf J, Li L, Litvinov P, Liu Y, Lopatin A, Marbach T, Maring H, Martins V, Meijer Y, Milinevsky G, Mukai S, Parol F, Qiao Y, Remer L, Rietjens J, Sano I, Stammes P, Stamnes S, Sun X, Tabary P, Travis LD, Waquet F, Xu F, Yan C, Yin D. Polarimetric remote sensing of atmospheric aerosols: Instruments, methodologies, results, and perspectives. *J Quant Spectrosc Radiat Transfer* 2019;224:474–511. doi:10.1016/j.jqsrt.2018.11.024.
- [6] ESA-DEIMOS, Earth Observation Mission CFI Software, Mission Specific Customizations, Code: EO-MA-DMS-GS-0018, Issue: 4.14, 2017.
- [7] ESA-DEIMOS, Earth Observation Mission CFI Software, Conventions Document, Code: EO-MA-DMS-GS-0001, Issue: 4.14, 2017a.
- [8] EUMETSAT. 4MSDS final project report, 2018 [https://www.eumetsat.int/website/wcm/idc/idcplg?IdcService=GET\\_FILE&dDocName&PDF\\_4MSDS\\_REP&RevisionSelectionMethod&LatestReleased&Rendition=Web](https://www.eumetsat.int/website/wcm/idc/idcplg?IdcService=GET_FILE&dDocName&PDF_4MSDS_REP&RevisionSelectionMethod&LatestReleased&Rendition=Web).
- [9] EUMETSAT. EPS-SG 3MI level 1C product user guide, EUM/LEO-EPSSG/DOC/16/893761 <ftp://ftp.eumetsat.int/pub/EPS/out/lang/3MI/L1C/>.
- [10] EUMETSAT. O2 A-band cloud top pressure retrieval with METimage, Final Report, 2018 [https://www.eumetsat.int/website/wcm/idc/idcplg?IdcService=GET\\_FILE&dDocName&PDF\\_SS\\_O2\\_CTP\\_METIMAGE\\_FIN\\_REP&RevisionSelectionMethod=LatestReleased&Rendition=Web](https://www.eumetsat.int/website/wcm/idc/idcplg?IdcService=GET_FILE&dDocName&PDF_SS_O2_CTP_METIMAGE_FIN_REP&RevisionSelectionMethod=LatestReleased&Rendition=Web).
- [11] Fougnie B, Bracco G, Lafrance B, Ruffel C, Hagolle O, Tinel C. PARASOL in-flight calibration and performance. *Appl Opt* 2007;46(22):5435–51.
- [12] Fougnie B, Marbach T, Lacan A, Lang R, Schlüssel P, Poli G, Munro R, Couto AB. The multi-viewing multi-channel multi-polarisation imager – Overview of the 3MI polarimetric mission for aerosol and cloud characterization. *J Quant Spectrosc Radiat Transfer* 2019;219:23–32.
- [13] Maignan F, Bréon FM, Lacaze R. Bidirectional reflectance of earth targets: evaluation of analytical models using a large set of spaceborne measurements with emphasis on the Hot Spot. *Remote Sens Environ* 2004;90:210–20.
- [14] Marbach T, Riedi J, Lacan A, Schlüssel P. The 3MI mission: multi-viewing-channel-polarisation imager of the EUMETSAT polar system: second generation (EPS-SG) dedicated to aerosol and cloud monitoring. In: *Polarization science and remote sensing VII*; 2015.
- [15] Parol P, Buriez JC, Vanbauce C, Riedi J, Labonnote LC, Doutriaux-Boucher M, Vesperini M, Seze G, Couvert P, Viollier M, Breon FM. Capabilities of multi-angle polarization cloud measurements from satellite: POLDER results. *Adv Space Res* 2004;33:1080–8.
- [16] Phillips P, Bonsignori R, Schlüssel P, Schmülling F, Spezzi L, Watts P, Zerfowski I. Overview of calibration and validation activities for the EUMETSAT polar system: second generation (EPS-SG) visible/infrared imager (METimage). In: *Sensors, Systems, and next-generation satellites xX*; 2016 1000005. doi:10.1117/12.2240938.
- [17] Schlüssel P, Kayal G. Introduction to the next generation EUMETSAT polar system (EPS-SG) observation missions. In: *Sensors, Systems, and next-generation satellites XXI*, 10423; 2017. p. 1–16.
- [18] Tancré D, Bréon FM, Deuzé JL, Dubovik O, Ducos F, François P, Goloub P, Herman M, Lifermann A, Waquet F. Remote sensing of aerosols by using polarized, directional and spectral measurements within the A-Train: the PARASOL mission. *Atmos Meas Tech* 2011;4:1383–95.
- [19] van Harten G, Snik F, Rietjens JHH, Smit JM, de Boer J, Diamantopoulou R, Hasekamp OP, Stam DM, Keller CU, Laan EC, Verlaan AL, Vliegthart WA, Ter Horst R, Navarro R, Wielinga K, Hannemann S, Moon SG, Voors R. Prototyping for the spectropolarimeter for planetary EXploration (SPEX): calibration and sky measurements. *Proc SPIE* 2011;8160. doi:10.1117/12.893741.
- [20] van Amerongen A, Rietjens J, Campo J, Dogan E, Dingjan J, Nalla R, Caron J, Hasekamp O. SPEXone: a compact multi-angle spectro-polarimeter. In: *Proceedings of the AGU conference*; 2018 Paper 378114.